# SARS-CoV-2 induces double-stranded RNA-mediated innate immune responses in respiratory epithelial derived cells and cardiomyocytes

Yize Li [a,z,*,#], David M Renner[a,z,*], Courtney E Comar [a,z,*], Jillian N Whelan[a,z,*], Hanako M Reyes[a,z] Fabian Leonardo Cardenas-Diaz[b,y], Rachel Truitt[b,x], Li Hui Tan[c], Beihua Dong[d], Konstantinos Dionysios Alysandratos[e], Jessie Huang[e], James N. Palmer[c], Nithin D. Adappa[c], Michael A. Kohanski[c], Darrell N. Kotton[e], Robert H Silverman[d], Wenli Yang[b], Edward Morrisey[b,y], Noam A. Cohen[c,f,g], Susan R Weiss [a,z,#, ^]

Departments of Microbiology[a], Medicine[b], Otorhinolaryngology[c], Institute for Regenerative Medicine[x], Penn Center for Research on Coronaviruses and Other Emerging Pathogens[z], Penn-CHOP Lung Biology Institute[y], Perlman School of Medicine at the University of Pennsylvania, Philadelphia, PA, 19104

[d]Department of Cancer Biology, Lerner Research Institute, Cleveland Clinic, Cleveland, OH 44195 USA

[e]Department of Medicine, the Pulmonary Center, Center for Regenerative Medicine Boston University School of Medicine, Boston, MA 02118, USA

[f]Corporal Michael J. Crescenz VA Medical Center, Philadelphia PA, 19104

[g]Monell Chemical Senses Center, Philadelphia, PA, 19104

#Address correspondence to: Susan R. Weiss, weisssr@pennmedicine.upenn.edu or Yize Li yizeli@pennmedicine.upenn.edu

^lead contact: Susan R. Weiss, weisssr@pennmedicine.upenn.edu

[*] These authors contributed equally to this work

**Summary**

Coronaviruses are adept at evading and/or antagonizing double-stranded RNA-induced host antiviral pathways, including interferon signaling, OAS-RNase L and PKR while robust cytokine responses characterize severe coronavirus disease. Knowledge of how newly emerged SARS-CoV-2 interacts with these pathways is minimal. SARS-CoV-2 readily infects patient-derived nasal epithelial cells and induced pluripotent stem cell-derived alveolar type 2 cells(iAT2) and cardiomyocytes(iCM). Robust activation of interferons or RNase L is not observed, while PKR activation is evident in iAT2 and iCM. In SARS-CoV-2 infected Calu-3 and A549$^{ACE2}$ lung derived cell lines, activation of all pathways is observed, similar to a mutant MERS-CoV lacking innate immune antagonists. Moreover, increased replication in *RNASEL* knockout A549$^{ACE2}$ cells, implicates RNase L in restricting SARS-CoV-2. Finally, while SARS-CoV-2 is less adept at antagonizing these host defense pathways compared to other coronaviruses, the innate immune response is still generally weak. These host-virus interactions may contribute to the unique pathogenesis of SARS-CoV-2.

**Keywords:** SARS-CoV-2; interferon, OAS-RNase L, PKR, viral accessory proteins

51 **Introduction**

52 Severe acute respiratory syndrome coronavirus (SARS-CoV)-2 emerged in China in late 2019,
53 causing the COVID-19 pandemic with extensive morbidity and mortality, leading to major changes
54 in day-to-day life in many parts of the world. This was the third lethal respiratory coronavirus, after
55 SARS-CoV in 2002 and Middle East respiratory coronavirus (MERS-CoV) in 2012, to emerge
56 from bats in the twenty first century. Although these viruses are all members of the
57 *Betacoronavirus* genus (Llanes et al., 2020), each has caused a somewhat different pattern of
58 pathogenesis and spread in humans (Fehr and Perlman, 2015); therefore it is important to
59 understand how these viruses interact with their host. Additionally, recent reports indicate that
60 ancestors of SARS-CoV-2 as well as other SARS-CoV-like viruses have been circulating in bats
61 for decades, suggesting potential future instances of direct spread to humans (Boni et al., 2020).
62

63 Coronaviruses are enveloped viruses with large, positive-sense single-stranded (ss)RNA
64 genomes of around 30kb that can infect a diverse range of mammals and other species.
65 Coronaviruses use much of their genomes, including their approximately 20 kb Orf1ab replicase
66 locus comprising the 5' two thirds of the genome, to encode proteins that antagonize host cell
67 responses (Perlman and Netland, 2009). As a result they are remarkably adept at antagonizing
68 host responses, in particular the double-stranded RNA (dsRNA)-induced pathways that are
69 essential components of the host innate immune response (Cruz et al., 2011; Dedeurwaerder et
70 al., 2014; Koetzner et al., 2010; Kopecky-Bromberg et al., 2007; Weiss and Navas-Martin, 2005).
71 In addition, interspersed among the structural genes encoded in the 3' third of the genome are
72 lineage-specific genes encoding accessory proteins, which are non-essential for RNA replication
73 and variable among CoV lineages that further divide the *Betacoronavirus* genus (Cui et al., 2019).
74 These accessory proteins often have functions in antagonizing host cell responses and thus likely
75 contribute to discrepancies in pathogenesis and tropism observed among the different lineages
76 (Comar et al., 2019; Kikkert, 2020; Zhao et al., 2012).

77

78 Like other RNA viruses, coronaviruses produce double-stranded RNA (dsRNA) early on during
79 the infection cycle as a result of genome replication and mRNA transcription (Sola et al., 2015).
80 Host cell pattern recognition receptors (PRRs) sense viral dsRNA as pathogenic non-self and
81 respond by activating several antiviral pathways critical for early defense against viral invasion.
82 DsRNA sensing by cytosolic PRRs can be divided into three key pathways – interferon (IFN)
83 production, ribonuclease L (RNase L) activation, and protein kinase R (PKR) activation (**Fig 1**)
84 (Hur, 2019). Detection of dsRNA by MDA5 during coronavirus infection (Roth-Cross et al., 2008),
85 leads to the production of type I ($\alpha/\beta$) and type III ($\lambda$) IFN. Upon binding to its specific cell surface
86 receptor, IFN triggers phosphorylation of STAT1 and STAT2 transcription factors, which then
87 induce expression of interferon stimulated genes (ISGs) with antiviral activities (Lopusna et al.,
88 2013; Platanias, 2005). In parallel, dsRNA is also sensed by oligoadenylate synthetases (OASs),
89 primarily OAS3, which synthesize 2',5'-linked oligoadenylates (2-5A)(Li et al., 2016; Whelan et
90 al., 2019). Generation of 2-5A induces dimerization and activation of ribonuclease L (RNase L),
91 leading to degradation of viral and host ssRNA. Finally, dsRNA sensing by protein kinase R (PKR)
92 will induce PKR autophosphorylation, permitting PKR to then phosphorylate the translation
93 initiation factor eIF2$\alpha$, which results in protein synthesis shutdown and restriction of viral
94 replication (Sadler and Williams, 2008). While RNase L and PKR antiviral activity are not
95 dependent on IFN production (Whelan et al., 2019), the genes encoding OASs and PKR are ISGs,
96 therefore these pathways can be activated and/or reinforced by IFN production. Similarly, RNase
97 L and PKR activation can promote IFN production, cellular stress, inflammation, and/or apoptotic
98 death (Banerjee et al., 2014; Castelli et al., 1997; Chakrabarti et al., 2015; Kang and Tang, 2012;
99 Malathi et al., 2007; Zhou et al., 1997), thus further reducing host cell viability.

100

101 Induction and inhibition of innate immune responses during infection with SARS-CoV-2 have yet

102 to be fully characterized. Furthermore, while it is well understood that SARS-CoV-2 enters the
103 human body through the upper respiratory tract, it is unclear which cell types of the upper and
104 lower respiratory system contribute to sustained infection and resulting disease in the airways
105 and elsewhere. We have performed SARS-CoV-2 infections of primary nasal epithelial cells,
106 induced pluripotent stem cell (iPSC)-derived alveolar type 2 cells (iAT2), and iPSC-derived
107 cardiomyocytes (iCM), which together represent the host tissues likely affected by clinical SARS-
108 CoV-2 infection (Hou et al., 2020; Sharma et al., 2020). We assessed viral replication in these
109 cell types as well as the degree of ensuing dsRNA-sensing responses. We also employed two
110 respiratory tract derived immune-competent cells lines, Calu-3 cells and A549 cells, to investigate
111 dsRNA-induced pathway activation during SARS-CoV-2 infection. In addition, we compared host
112 responses to SARS-CoV-2 with those of MERS-CoV and MERS-CoV-ΔNS4ab, a mutant lacking
113 expression of two dsRNA-induced innate immune pathway antagonists that we have
114 characterized previously (Comar et al., 2019).
115
116 **Results**
117
118 **SARS-CoV-2 replicates efficiently in cells derived from upper and lower respiratory tract.**
119 We compared the replication of SARS-CoV-2 and MERS-CoV in nasal epithelia-derived cells, a
120 relevant site of infection *in vivo*, from four different donors (**Fig 2A**). For each virus, replication
121 was similar in cells from all four individuals, although the extent of replication was somewhat
122 variable. The trends in replication kinetics, however, were significantly different between SARS-
123 CoV-2 and MERS-CoV infections. Replication of SARS-CoV-2 increased until 96hpi, but then
124 plateaued at nearly $10^6$ plaque-forming units (PFU)/ml. MERS-CoV replication peaked at 96hpi,
125 at a lower titer than SARS-CoV-2. Nasal epithelial cell cultures were stained with antibodies to
126 identify ciliated cells (anti-type IV β-tubulin), a key feature of this cell type, and either SARS-CoV-
127 2 or MERS-CoV nucleocapsid expression (anti-N protein) (**Fig 2B**). We detected abundant N
128 expressed in both SARS-CoV-2 and MERS-CoV infected cells, indicating that these cells were

129 sufficiently infected at 48 hours post infection (hpi). Interestingly, robust replication occurred in
130 these cultures, despite a very low level of ACE2 protein expression in cells from the three
131 individuals examined (**Fig 2C**).
132
133 We measured dsRNA-induced host responses to SARS-CoV-2 infection, including type I and type
134 III IFN mRNA induction, RNase L activation, and PKR activation, in the nasal cells. For RT-qPCR
135 analysis, we extracted RNA from SARS-CoV-2 infected cultures from four different donors at
136 120hpi. We verified that virus was replicating by quantifying viral genome copies from intracellular
137 RNA (**Fig S1A**). We then quantified mRNA expression of IFN-β (type I IFN), IFN-λ (type III IFN),
138 select ISGs induced downstream of IFN production (*OAS2*, *IFIT1*, *IFIH1*), and the neutrophil
139 attracting chemokine IL-8 (*CXCL8*), which has been implicated in nasal inflammation during viral
140 infection (Mukaida, 2003; Turner et al., 1998) (**Fig 2D**)**.** The data shown represents the average
141 of cells from three donors. There was some induction of type I and to a lesser extent type III IFN
142 mRNA, and minimal induction of the ISG mRNAs examined. Similarly, *CXCL8* encoding IL-8 was
143 barely induced. Interestingly, this may be at least partially due to high basal levels of IFN (notably
144 IFN-λ) and ISG (notably OAS2) mRNAs compared with other cell types examined below, which
145 would result in reporting of weak fold changes in mRNA levels compared with mock infected cells
146 (**Fig S2**). To further investigate this very weak ISG induction, using cells from the same donors
147 as the IFN/ISG mRNA quantification, we assessed the phosphorylation of STAT1, a transcription
148 factor that is itself encoded by an ISG, which is primarily a key mediator of type I and type III IFN
149 signaling. Upon infection, STAT1 is phosphorylated before complexing with STAT2 and IRF9 to
150 form ISGF3, which translocates to the nucleus where it mediates the activation of ISG
151 transcription (Stark and Darnell, 2012). Consistent with the weak activation of ISGs, there was no
152 evidence of phosphorylation of STAT1, likely due to low levels or transient phosphorylation (**Fig**
153 **2C**). In addition, we did not detect PKR activation, as indicated by the absence of phosphorylated

154 PKR and eIF2α in SARS-CoV-2 infected cells, while PKR and eIF2α were clearly expressed (**Fig**
155 **2C**). We also assessed activation of the OAS-RNase L pathway during SARS-CoV-2 infection of
156 cells from two of the same four donors. Since 28S and 18S ribosomal RNAs (rRNAs) are targeted
157 for degradation by activated RNase L, we can evaluate 28S and 18S rRNA integrity using a
158 Bioanalyzer as a readout for RNase L activation. The absence of any rRNA degradation in SARS-
159 CoV-2 infected cells (**Fig 2E**) indicated that RNase L was not activated despite abundant RNase
160 L protein expression (**Fig 2C**).
161
162
163 Next, we sought to examine host innate immune responses during infection of alveolar type 2
164 cells (AT2), a major target of SARS-CoV-2 infection in humans (Hou et al., 2020; Ng et al., 2016;
165 Qian et al., 2013). Initially, we attempted infections in lung organoid cultures, however they were
166 not sufficiently permissive to SARS-CoV-2. Thus, we employed induced pluripotent stem cell
167 (iPSC)-derived iAT2 cells (SPC2 line), expressing tdTomato from the endogenous locus of
168 surfactant protein-C (SFTPC), an AT2 cell specific marker (Jacob et al., 2019). As in nasal cells,
169 virus replicated efficiently, reaching a titer of $10^6$ PFU/ml by 48hpi (**Fig 3A**). Staining of cultures
170 with an anti-N antibody showed that most of the iAT2 cells were infected, without obvious
171 cytopathic effect (CPE) during infection (**Fig 3B**). Notably, SARS-CoV-2 infection of iAT2 cells
172 was robust despite ACE2 expression being below the level of detection by immunoblotting (**Fig**
173 **3C**). We observed activation of the PKR pathway as indicated by both PKR and eIF2α
174 phosphorylation by immunoblotting (**Fig 3C**). We extracted RNA from infected iAT2 cells for RT-
175 qPCR analysis, verified these cells were replicating virus by quantifying genome RNA copies (**Fig**
176 **S1B**), and assessed IFN/ISG induction. As with the nasal cells, we observed weak induction of
177 IFN-β and IFN-λ mRNA from mock infected and infected cells (**Fig 3D**), while MDA5 (Roth-Cross
178 et al., 2008) a dsRNA sensor in the pathway leading to IFN production during coronavirus
179 expression, is not detected (**Fig 3C)**. We used the alphavirus Sindbis virus (SINV) as a positive

180 control, which we have previously shown induces robust activation of all dsRNA-induced
181 pathways (Comar et al., 2019). Surprisingly, we observed greater increases in OAS2 and IFIT
182 mRNA expression by SARS-CoV-2 compared with SINV (**Fig 3D**), but with minimal induction of
183 IFIH1 mRNA or protein (MDA5) (**Fig 3C&D)**. However, we did not observe phosphorylation of
184 STAT1 (**Fig 3C**), as in the nasal cells above. Additionally, we did not observe any degradation of
185 rRNA in SARS-CoV-2 infected cells, and only slight degradation by SINV despite ample
186 expression of RNase L (**Fig 3E**), suggesting minimal activation of RNase L in iAT2 cells in general.
187
188 **SARS-CoV-2 replicates and induces innate immune responses in iPSC-derived**
189 **cardiomyocytes.** Since many COVID-19 patients experience cardiovascular symptoms and
190 pathology (Lindner et al., 2020; Shi et al., 2020), we investigated SARS-CoV-2 infection of iPSC
191 derived-cardiomyocytes (iCM). SARS-CoV-2 replicated robustly in these cells reaching titers of
192 approximately $10^6$ PFU/ml by 48hpi (**Fig 4A**), similar to replication in nasal and iAT2 cells. Cells
193 were stained with an antibody against cardiac troponin-T (cTnT) as a marker for cardiomyocytes,
194 and an antibody against the viral N protein to identify infected cells (**Fig 4B**). In addition, we
195 detected clear cytopathic effect (CPE), in iCM, which differed from infected nasal and iAT2 cells.
196 This CPE included syncytia resulting from cell-to-cell fusion, which is typical of coronaviruses and
197 a result of intracellular cleavage of the viral spike protein by the host enzyme furin (Belouzard et
198 al., 2009; de Haan et al., 2004; Gombold et al., 1993; Qiu et al., 2006; Yamada and Liu, 2009).
199 Interestingly, while we observed detectable ACE2 protein expression in mock infected cells in two
200 independent experiments, we observed loss of ACE2 expression upon SARS-CoV-2 infection,
201 consistent with a recent study (Sharma et al., 2020) (**Fig 4C**)**.** We extracted RNA from mock
202 infected cells and cells infected with SARS-CoV-2 or SINV, verified that virus was replicating by
203 quantifying viral genome in intracellular RNA (**Fig S1C**), and quantified expression of mRNAs for
204 IFNs and select ISGs. We found low levels of IFN/ISGs transcript in iCM similar to the nasal and
205 iAT2 cells (**Fig D**), perhaps due to the undetectable levels of MDA5 and MAVS protein expression

206 in these cells (**Fig 4C**). SINV also induced host mRNAs weakly, with the exception of IFN-λ, in
207 these cells (**Fig 4D**). We observed no degradation of rRNA, suggesting an absence of RNase L
208 activation in iCM with SARS-CoV-2 or SINV (**Fig 4E**), despite clear infection with either virus (**Fig**
209 **S1C**). This was not surprising as there was no RNase L detectable by immunoblot in these cells
210 (**Fig 4C**). Finally, as in iAT2 cells, we observed phosphorylation of PKR and eIF2α, indicating that
211 the PKR antiviral pathway is activated (**Fig 4C**).
212
213
214 **SARS-CoV-2 replicates in respiratory epithelial cell lines and induces dsRNA responsive**
215 **pathways.**
216
217 We aimed to further characterize the relationship between SARS-CoV-2 and dsRNA-induced host
218 response pathways, which were activated to variable levels in the different primary and iPSC
219 derived cells evaluated. We chose two respiratory epithelium-derived human cell lines, A549 and
220 Calu-3, both of which are immune competent and have been used for studies of SARS-CoV
221 (Blanco-Melo et al., 2020) and MERS-CoV (Comar et al., 2019; Thornbrough et al., 2016). A549
222 cells were not permissive to SARS-CoV-2, which correlated with undetectable levels of the SARS-
223 CoV-2 receptor ACE2 (**Fig S3**). Therefore, we generated A549 cells expressing the ACE2
224 receptor ($A549^{ACE2}$) by lentiviral transduction, and used two single cell clones, C44 and C34, for
225 all experiments (**Fig S3**). Both $A549^{ACE2}$ clones express high levels of ACE2 greater than the
226 endogenously expressed ACE2 in Calu-3 cells (**Fig S3**) and in the primary cells discussed above
227 (**Fig 2-4**).
228
229 We performed single step growth curves to measure replication of SARS-CoV-2 over the course
230 of one infectious cycle in $A549^{ACE2}$ cells, simian Vero-E6 cells, which are commonly used to
231 prepare SARS-CoV-2 stocks, and Calu-3 cells (clone HTB-55). SARS-CoV-2 replicated robustly
232 in $A549^{ACE2}$ and Vero-E6 cells (**Fig 5A**) but in comparison viral yields were lower in Calu-3 cells
233 (**Fig 5B**). Since Calu-3 cells also support MERS-CoV infection, we compared SARS-CoV-2

234 replication to that of MERS-CoV (WT) and MERS-CoV-ΔNS4ab, a mutant deleted in host cell
235 antagonists NS4a, a dsRNA-binding protein, and NS4b, a 2'5'-phosphodiesterase that prevents
236 RNase L activation and nuclear translocation of NF-κB (Canton et al., 2018; Comar et al., 2019).
237 Consistent with our previous work (Comar et al., 2019), MERS-CoV-ΔNS4ab reduced viral titers
238 from WT MERS-CoV levels, although they remained higher than SARS-CoV-2 titers (**Fig 5B**). To
239 further understand the replication of SARS-CoV-2, we stained A549, Calu-3 and Vero-E6 cells at
240 24 hpi with antibodies against viral N protein and viral dsRNA, including additional Calu-3 staining
241 at 48 hpi since replication kinetics are slower (**Fig 5C**). We observed cytopathic effect in all three
242 cell types, with N staining in the cytoplasm. Syncytia were observed in $A549^{ACE2}$ and Calu-3 cells,
243 but not in Vero cells (**Fig 5C**). We also observed viral dsRNA localized to perinuclear foci as we
244 and others have described during infection with other coronaviruses (Comar et al., 2019; Knoops
245 et al., 2008; Lundin et al., 2014; Rabouw et al., 2016).
246
247 We used RT-qPCR to quantify the induction of type I and type III IFNs and select ISGs at 24 and
248 48 hpi (**Fig 6A**), as well as the intracellular viral genome copies to verify replication (**Fig 6B**) in
249 $A549^{ACE2}$ cells. Using SINV as a positive control, we found relatively low levels of both IFNβ and
250 IFNλ mRNA at 24 and 48 hpi by SARS-CoV-2, compared to SINV (**Fig 6A**). Notably, IFN induction
251 was greater than observed in the nasal, iAT2, or iCM cells, possibly due to lower basal levels of
252 IFNβ, but not IFNλ, mRNA in the $A549^{ACE2}$ cells, which allow for greater fold changes over mock
253 infected cells (**Fig S2**). As observed previously with SINV and MERS-CoV, SARS-CoV-2 induced
254 more IFNλ than IFNβ, typical of A549 cells (Comar et al., 2019). Levels of ISG mRNAs were
255 variable, with SARS-CoV-2 inducing moderate levels of OAS2 and IFIT1 mRNAs, but only late in
256 infection (48 hpi), similar to those induced by SINV at 24 hpi **(Fig 6A**). We observed minimal
257 effects on mRNA levels of IFIH1 and the cytokine CXCL8 at both timepoints (**Fig 6A**).
258 Furthermore, we did not detect any STAT1 phosphorylation at 24 hpi (**Fig 6C**), which correlates

259 with weak ISG expression, suggesting defective IFN signaling downstream of IFN production. The
260 data shown in Fig 6 were derived from A549$^{ACE2}$ clone C44; similar data were obtained for a
261 second clone, C33 **(Fig S4)**.
262
263 We evaluated IFN/ISG responses in Calu-3 cells, which provided a second lung-derived cell line
264 that additionally supports both SARS-CoV-2 and MERS-CoV infection, allowing us to compare
265 host responses between the two lethal CoVs. We compared SARS-CoV-2 responses to both WT
266 MERS-CoV and mutant MERS-CoV-ΔNS4ab (**Fig 7A**). Although we observed reduced MERS-
267 CoV-ΔNS4ab infectious virus production compared with WT MERS-CoV (**Fig 5B**), we detected
268 similar intracellular viral genome levels of all three viruses (**Fig 7B**). We found previously that
269 MERS-CoV-ΔNS4ab induces higher levels of IFNs and ISGs compared to WT MERS-CoV, and
270 also activates RNase L and PKR (Comar et al., 2019). Herein, in Calu-3 cells, we observed
271 greater SARS-CoV-2 induction of IFN mRNAs as compared to A549$^{ACE2}$ cells (**Fig 6A&S4B**).
272 Interestingly, SARS-CoV-2 induced higher IFN mRNA levels than WT MERS-CoV at 24 and 48
273 hpi, which more closely resemble those induced by the IFN antagonist-deficient mutant MERS-
274 CoV-ΔNS4ab by 48hpi (**Fig 7A**). Similarly, SARS-CoV-2 generally induced more ISG mRNA than
275 WT MERS-CoV, and even more OAS2 mRNA than MERS-ΔNS4ab (**Fig 7A**). Induction of CXCL8
276 was weak for all viruses (**Fig 7A**). Notably, SARS-CoV-2 induced ISG mRNAs in Calu-3 (24hpi)
277 without the delay observed in A549$^{ACE2}$ cells. Consistent with earlier ISG mRNA induction during
278 infection, SARS-CoV-2 infection promotes phosphorylation of STAT1 in Calu-3 cells (**Fig 7C**) as
279 recently reported (Lokugamage et al., 2020). SARS-CoV-2 induction of pSTAT1 as well as rapid
280 IFIT1 and OAS2 mRNA induction suggests a similar host response to SARS-CoV-2 as that
281 observed during mutant MERS-CoV-ΔNS4ab infection, and not that of WT MERS-CoV infection.
282
283 **SARS-CoV-2 infection activates RNase L and PKR.** We assessed activation of the RNase L
284 pathway by analyzing intracellular rRNA from infected cells for RNA integrity, as described above.

285 We found that SARS-CoV-2 promotes rRNA degradation minimally at 24 hpi and more clearly at
286 48 hpi in A549$^{ACE2}$, using SINV as a positive control (**Fig 8A**). Evaluation of RNase L activation in
287 SARS-CoV-2, WT MERS-CoV, and MERS-CoV-ΔNS4ab infected Calu-3 cells showed SARS-
288 CoV-2 activation of RNase L to a similar extent as MERS-CoV-ΔNS4ab, which lacks both a
289 dsRNA binding protein and a RNase L-specific antagonist (Comar et al., 2019; Siu et al., 2014)
290 (**Fig 8B**). In contrast, as we previously reported, WT MERS-CoV failed to activate RNase L
291 (Comar et al., 2019; Thornbrough et al., 2016) (**Fig 8B**). We also observed activation of PKR as
292 indicated by phosphorylation of PKR and downstream eIF2α, in both A549$^{ACE2}$ cells (**Fig 8C**) and
293 Calu-3 cells (**Fig 8D**) infected with SARS-CoV-2. In Calu-3 cells, SARS-CoV-2 induced PKR
294 phosphorylation to a similar extent as MERS-CoV-ΔNS4ab, while WT MERS-CoV failed to induce
295 a response**.** These data are consistent with IFN/ISG induction data described above, suggesting
296 that SARS-CoV-2 may not antagonize dsRNA pathways as efficiently as MERS-CoV, but instead
297 induces host responses similar to those observed during MERS-CoV-ΔNS4ab infection.
298
299 The A549$^{ACE2}$ cells were valuable in that they provided a system with intact innate immune
300 responses that was also amenable to CRISPR-Cas9 engineering. Thus, we used the A549$^{ACE2}$
301 cells to construct additional cell lines with targeted deletions of *MAVS*, *RNASEL*, or *PKR*, as we
302 have done previously for parental A549 cells (Li et al., 2017; Li et al., 2016). We could then use
303 these cells to determine whether activation of IFN, RNase L, and/or PKR resulted in attenuation
304 of SARS-CoV-2 replication (Li et al., 2017; Li et al., 2016). We validated the knockout (KO)
305 A549$^{ACE2}$ cell lines by western blot (**Fig 9A**) and compared replication of SARS-CoV-2 in *MAVS*
306 KO, *RNASEL* KO and *PKR* KO cells with levels in WT A549$^{ACE2}$ cells (**Fig 9B**). Interestingly, there
307 was little effect on SARS-CoV-2 replication with MAVS or PKR expression absent. In *RNASEL*
308 KO cells at 48 hpi, virus replication was two- to four-fold higher compared to WT A549$^{ACE2}$ cells
309 **(Fig 9B**). While the difference in replication between *RNASEL* KO and WT was not extensive, it

310 was statistically significant in three independent experiments. Additionally, infected *RNASEL* KO
311 cells exhibited strikingly more CPE as compared with WT, *PKR* KO, or *MAVS* KO cells, as
312 demonstrated by crystal violet-staining of infected cells (**Fig 9C**). We also assessed rRNA
313 degradation and, as expected, found that rRNA remained intact in the *RNASEL* KO A549$^{ACE2}$
314 cells, which further validated these cells. However, rRNA was degraded in *PKR* or *MAVS* KO
315 cells, indicating RNase L activation in both of these cell types (**Fig 9D**). These data are consistent
316 with our previous findings that activation of the RNase L pathway does not depend on MAVS
317 signaling in A549 cells infected with SINV or Zika virus (ZIKV) (Li et al., 2019; Whelan et al.,
318 2019). RNase L activation instead occurs in parallel with IFN production (**Fig 1**), and is likely
319 dependent on basal levels of OAS gene expression (Birdwell et al., 2016).
320
321
322
323 **Discussion**
324
325 SARS-CoV-2 is the causative agent of the severe acute respiratory, COVID-19. SARS-CoV-2
326 infection begins in the ciliated cells of the nasal epithelium and spreads to the lower respiratory
327 tract, possibly by aspiration of infectious nasal secretions, infecting alveolar type 2 (AT2) cells
328 and causing acute respiratory distress syndrome (ARDS) (Hou et al., 2020). Despite this typical
329 axis of infection, many infected individuals exhibit symptoms and pathology in other organ
330 systems, including the cardiovascular system (Puelles et al., 2020; Shi et al., 2020). Here, we
331 present data expanding our understanding of cellular responses from each one of these critical
332 areas. We focused on understanding the early host-viral interactions that trigger activation of the
333 dsRNA-sensing pathways, including the RNase L, PKR, and type I and III IFN pathways. We
334 evaluated responses to SARS-CoV-2 infection in primary nasal epithelia-derived upper airway
335 cells and iPSC-derived type II airway (iAT2) cells, which represent major sites of infection during
336 COVID-19 disease, as well as iPSC-derived cardiomyocytes (iCM), another likely target of
337 infection (Sharma et al., 2020). To complement these studies, we used two lung derived

338 transformed cell lines, Calu-3 cells and two different A549$^{ACE2}$ clones, to more mechanistically
339 dissect activation and antagonism of these pathways by SARS-CoV-2. We found that the extent
340 of IFN induction and signaling is variable among the primary cell types and cell lines used, but is
341 consistently only poorly induced. Interestingly, we show that SARS-CoV-2 infection results in
342 more IFN signaling (phosphorylation of STAT1 and IFN/ISG expression) when compared to
343 MERS-CoV in Calu-3 cells. We also found that SARS-CoV-2 activates RNase L and PKR in both
344 cell lines used and PKR in iAT2 cells and iCM, but not in primary nasal cells. Using KO cell lines,
345 we demonstrate that RNase L expression significantly impacts SARS-CoV-2 viral titers and CPE
346 observed during infection. These data suggest that while SARS-CoV-2 is generally a weak
347 activator of dsRNA-induced responses in cells of the respiratory and cardiovascular systems,
348 SARS-CoV-2 is less adept at antagonizing host responses than MERS-CoV.
349
350 Nasal cells are the initial replication site of SARS-CoV-2 and MERS-CoV. In quantifying virus
351 replication in infected nasal cell culture, we found that SARS-CoV-2 replicates to higher titer than
352 MERS-CoV, and the time period for shedding of virus is much longer (**Fig 2A**). We suggest that
353 this longer period of replication in nasal cells and stronger immune responses in Calu-3 cells may
354 in part explain why SARS-CoV-2 is less virulent, yet more contagious than MERS-CoV. Indeed
355 for SARS-CoV-2, $R_0$=5.7 (Sanche et al., 2020) while for MERS-CoV, ($R_0$=0.45)(Oh et al., 2016).
356
357 Infection of all three primary cell types – nasal cells, iAT2 cells, and iCM – resulted in high levels
358 of SARS-CoV-2 replication, while only cardiomyocytes exhibited obvious CPE (**Figs 2-4**). It was
359 easily observed with syncytia formation in both lines, but the kinetics of viral spread were slower
360 in Calu-3 (**Fig 5**). IFA staining with viral dsRNA-specific antibody (J2) showed SARS-CoV-2
361 dsRNA localized to perinuclear areas in A549$^{ACE2}$ and Calu-3 cells, which is typical of coronavirus
362 infection (**Fig 5**). The protein expression level of the SARS-CoV-2 host receptor ACE2 (Lu et al.,
363 2020; Wan et al., 2020; Zhou et al., 2020) in primary cells and Calu-3 cells was either low or

364 undetectable, indicating that high levels of receptor are not necessary for productive infection (**Fig**
365 **2-4&S3**). This is similar to previous observations in the murine coronavirus (MHV) system where
366 viral receptor CEACAM1a is very weakly expressed in the mouse brain, a major site of infection,
367 and particularly in neurons, the most frequently infected cells, as measured by RT-qPCR for
368 mRNA and antibody staining for protein (Bender et al., 2010).
369
370 The canonical IFN production and signaling pathways activated by the sensing of dsRNA, an
371 obligate intermediate in viral genome replication and mRNA transcription, provide a crucial early
372 antiviral response (**Fig 1**). The role of IFN responses during coronavirus infection is complex and
373 at times contradictory. For example, SARS-CoV induces poor IFN signaling during early infection
374 in mice, and treatment with IFN improves outcome. However, IFN production later in infection has
375 a pathogenic effect (Channappanavar and Perlman, 2017). Similarly, weak IFN responses have
376 been observed during initial stages of SARS-CoV-2 infection, but IFN produced later may
377 contribute to the strong inflammatory responses and resulting immunopathology observed during
378 SARS-CoV-2 infection cytokine storms (Giamarellos-Bourboulis et al., 2020; Hadjadj et al., 2020).
379 Furthermore, murine coronavirus (MHV) induces minimal levels of IFN in cell culture and *in vivo*,
380 yet IFN$\alpha/\beta$ receptor (IFNAR) KO mice lacking type I IFN signaling responses experience ectopic
381 virus spread and rapid death (Roth-Cross et al., 2008).
382
383 While IFNs may contribute to pathogenesis later on in infection, coronaviruses, including the lethal
384 human viruses, often prevent these responses early on during infection in both animal models
385 and humans (Arabi et al., 2017; Channappanavar et al., 2016; Channappanavar et al., 2019).
386 Antagonism of dsRNA-induced antiviral pathways has been well characterized for lineage a
387 betacoronaviruses (subgenera embeco; for example, murine coronavirus MHV) (Zhao et al.,
388 2012) and lineage c betacoronaviruses (merbeco; MERS-CoV and other related bat viruses)
389 (Comar et al., 2019), however there is less known about lineage b (sarbeco) betacoronaviruses,

390 including SARS-CoV (2002) and SARS-CoV-2. A recent report described a cohort of COVID-19
391 patients with impaired IFN and innate immune responses that correlated with enhanced disease
392 severity, suggesting that subversion of these host responses is important for severe SARS-CoV-
393 2-mediated clinical outcomes (Hadjadj et al., 2020). Thus, it is important to understand the basic
394 biology of SARS-CoV-2 interaction with the host innate immune system.
395
396 We and others have previously found that both MHV (lineage a) and MERS-CoV (lineage c)
397 betacoronaviruses induce only minimal type I and type III IFNs, and fail to activate RNase L or
398 PKR pathways (Rabouw et al., 2016; Thornbrough et al., 2016; Ye et al., 2007; Zhao et al., 2012;
399 Zhao et al., 2011). We found that SARS-CoV-2, like other betacoronaviruses, induced limited
400 amounts of type I and type III IFN mRNAs, although this was somewhat variable among the cell
401 types examined. Using SINV as a control for robust activation of IFN, we detected low levels of
402 type I and type III IFN mRNA in nasal cell, iAT2 cells, and iCM (**Fig 2-4**). However, we observed
403 higher levels of OAS2, an ISG, relative to SINV in iAT2 cells (**Fig 3D**). As we have observed
404 among murine cells, we saw vastly different levels of basal expression of both IFN and ISG
405 mRNAs among the cell types infected (**Fig S2**) (Li and Weiss, 2016; Zhao et al., 2013; Zhao et
406 al., 2011). It is understood that higher basal levels of innate immune response mRNAs typically
407 result in a lower threshold for activation of corresponding responses. Interestingly, we observed
408 significantly higher basal levels, especially IFNλ, in (uninfected) nasal cells as compared to iAT2
409 cells and iCM (**Fig S2A**). As major barrier cells, we speculate that this may be important for
410 protection as these cells are more exposed to infectious agents in the environment. Indeed, it is
411 well documented that type III IFNs serve as an added defense for epithelial cells, which may
412 perhaps explain some of the differences observed in basal gene expression between nasal cells
413 and iCM (Ank et al., 2008; Forero et al., 2019; Galani et al., 2017). As previously reported in heart
414 tissue, the iCM expressed undetectable levels of both MAVS and RNase L, (Uhlén et al., 2015;
415 Zhou et al., 1997), which is possibly to protect the heart from excessive inflammation.

416

417 In A549$^{ACE2}$ cells, SARS-CoV-2 induced low levels of IFNλ and IFNβ mRNAs and somewhat
418 higher ISG mRNA by 48 hpi, as compared with SINV (**Fig 6A**). We observed greater increases
419 in IFN induction in Calu-3 compared to A549$^{ACE2}$ (**Fig 7A**), which may be at least partially due to
420 higher basal levels of IFNs in the Calu-3 cells (**Fig S2**). Calu-3 cells were employed to directly
421 compare the host response to SARS-CoV-2 infection with that of MERS-CoV and mutant MERS-
422 CoV-ΔNS4ab, which lacks the NS4a and NS4b proteins that inhibit IFN production and signaling
423 (Canton et al., 2018; Comar et al., 2019; Rabouw et al., 2016). In Calu-3 cells, SARS-CoV-2
424 induced more IFN mRNA than WT MERS-CoV, closer to the level of MERS-CoV-ΔNS4ab (**Fig**
425 **7A**). Furthermore, SARS-CoV-2 induced higher levels of ISG mRNAs than MERS-CoV and, in
426 the case of OAS2, higher than MERS-CoV-ΔNS4ab as well. Consistent with this, in Calu-3 cells
427 SARS-CoV-2 and MERS-CoV-ΔNS4ab, but not WT MERS-CoV, promoted STAT1
428 phosphorylation (**Fig 7C**), which leads to ISG transcription and antiviral responses. Overall, our
429 results displayed a trend of relatively weak IFN responses induced by SARS-CoV-2 in airway
430 epithelial cells with limited ISG induction, when compared with host responses to viruses from
431 other families. Additionally, our data show that enhanced IFN/ISG responses in Calu-3 cells
432 restrict virus production, while lower host responses in A549$^{ACE2}$ cells correlate with higher viral
433 titers (**Fig 5**). Considering how robust ACE2 expression appears dispensable for infection of
434 some cell types (nasal, iAT2, Calu-3), these data also indicate that stronger innate immune
435 responses may be more effective at restricting SARS-CoV-2 replication than low ACE2
436 expression level.

437

438 We found that SARS-CoV-2 was unable to prevent activation of RNase L and PKR, although to
439 different extents among the cell types, unlike two other betacoronaviruses, MHV and MERS-CoV,
440 which shut down these pathways (Comar et al., 2019; Ye et al., 2007; Zhao et al., 2012). We

441 observed PKR activation as indicated by phosphorylation of PKR and eIF2α in SARS-CoV-2
442 infected iAT2 (**Fig 3C**) and iCM (one/two experiments) (**Fig 4C**), but not in nasal cells (**Fig 2C**).
443 However, we did not detect rRNA degradation indicative of RNase L activation in these cell types
444 (**Fig 2E, 3E, 4E**). Activation of both RNase L and PKR were observed in A549$^{ACE2}$ and Calu-3
445 cells during infection with SARS-CoV-2 (**Fig 8**). In Calu-3 cells, this contrasted MERS-CoV and
446 was more similar to MERS-CoV-ΔNS4ab. Previous studies have shown that MERS-CoV NS4a
447 restricts phosphorylation of PKR by binding dsRNA, reducing its accessibility to PKR (Comar et
448 al., 2019; Rabouw et al., 2016). Additionally, MERS-CoV NS4b, a 2'-5' phosphodiesterase,
449 prevents RNase L activation by degrading 2-5A, the small molecular activator of RNase L (Comar
450 et al., 2019; Thornbrough et al., 2016). Current understanding of SARS-CoV-2 protein function
451 infers an absence of these types of protein antagonists, therefore it is not surprising that both of
452 these pathways are activated during infection of both A549$^{ACE2}$ and Calu-3. Indeed, MERS-CoV-
453 ΔNS4ab attenuation compared to WT MERS-CoV, as well as lower SARS-CoV-2 titers than those
454 of MERS-CoV (**Fig 5B**), may be at least in part due to RNase L and PKR activation in addition to
455 IFN/ISG induction in Calu-3 cells.
456
457 Consistent with previous studies involving the alphavirus SINV, we found that neither MERS-CoV-
458 ΔNS4ab nor SARS-CoV-2 activated dsRNA-induced pathway responses as robustly as SINV (Li
459 et al., 2016; Whelan et al.). We suggest this may be due to CoV antagonists encoded by the nsp
460 genes of the replicase locus. For CoVs, conserved replicase proteins have been identified as
461 important modulators of innate immune invasion, including nsp1, nsp14, nsp15, and nsp16
462 (Gordon et al., 2020; Kindler et al., 2017; Perlman and Netland, 2009; Volk et al., 2020). Most
463 notably, nsp15 encodes an endoribonuclease (EndoU) that has been shown in the MHV system
464 to restrict dsRNA accumulation and thus limit activation of both RNase L and PKR (Deng et al.,
465 2017; Kindler et al., 2017). A very recent report using a replicon system concludes that SARS-

466 CoV-2 nsp1 and nsp6 are more effective antagonists than the homologous proteins of SARS-CoV
467 or MERS-CoV (Xia et al., 2020). Nevertheless, increased, albeit modest, replication and
468 enhanced cell death in SARS-CoV-2 infected *RNASEL* KO cells indicates that this pathway is
469 activated and indeed restricts replication and downstream cell death caused by SARS-CoV-2
470 infection (**Fig 9B&C**). In contrast, we found that *PKR* KO had no effect on viral titer. This is
471 consistent with our previous finding that MERS-CoV infection inhibits host protein synthesis
472 independent of PKR, so that PKR phosphorylation during MERS-CoV-ΔNS4ab infection did not
473 lead to further reduction (Comar et al., 2019). Finally, KO of *MAVS* and the consequent loss of
474 IFN production had no significant effect on viral titer or cell death. This is similar to our previous
475 findings demonstrating that RNase L activation can occur independent of virus-induced IFN
476 production with other viruses (SINV) (Li et al., 2019) and ZIKV (Whelan et al., 2019) in A549
477 cells, as well as for MHV in murine bone marrow-derived macrophages (Birdwell et al., 2016).
478 This underscores the importance of the RNase L and PKR antiviral pathways, which can be
479 activated early in infection upon concurrent dsRNA sensing by OAS, PKR, and MDA5 receptors
480 before IFN is produced. Alternatively, these pathways can be activated in cells infected by virus
481 that produce low levels of IFN only late in infection, as we observe here with SARS-CoV-2. Further
482 studies are required to determine whether activation of PKR or RNase L during SARS-CoV-2
483 infection results in functional outcomes characteristic of these pathways, including inhibition of
484 protein synthesis, induction of apoptosis, cleavage of viral RNA, or induction of inflammatory
485 responses (**Fig 1**). Interestingly, we observed possible RNase L-induced apoptosis in the SARS-
486 CoV-2 infected A549$^{ACE2}$ WT, *MAVS* KO, and *PKR* KO cells, when compared with mock infected
487 counterparts (**Fig 9C**). However, *RNASEL* KO cells displayed the most cell death among the four
488 cell lines, suggesting that virus-induced cell lysis in the *RNASEL* KO cells where viral titers are
489 highest (**Fig 9B**) is more detrimental to cells than RNase L-induced programmed cell death.
490

491 There have been few studies on the interaction of the prototype lineage b betacoronavirus,
492 SARS-CoV (2002), with these dsRNA-induced pathways, with most of the studies describing IFN
493 antagonists involving overexpressed protein and overexpressed artificial IFN promoter
494 sequences for readouts. In this way, it was reported that Orf3b, Orf6 and nucleocapsid (N) protein
495 are antagonists of IFN production and signaling (Kopecky-Bromberg et al., 2007). The role of the
496 SARS-CoV Orf6 encoded protein as an IFN antagonist was subsequently confirmed in the context
497 of virus infection, and further defined as Orf6 binding to host nuclear importins to prevent
498 translocation of STAT1 and other transcription factors, thus impairing induction of antiviral ISGs
499 (Frieman et al., 2007; Sims et al., 2013). SARS-CoV-2 encodes an Orf6 protein with 69%
500 homology to SARS-CoV Orf6 (Lokugamage et al., 2020), as well as a similar, truncated Orf3b
501 which has been shown by overexpression studies to antagonize IFN mRNA transcription (Konno
502 et al., 2020). Strikingly, recent work using overexpression systems of SARS-CoV-2 Orf6 found
503 that it interacts with host KPNA2, the same target of the SARS-CoV Orf6 protein (Xia et al., 2020).
504 However, further investigation is required to determine how similarly the proteins from the two
505 viruses function in the context of infection.
506
507 We have shown that SARS-CoV-2 activates dsRNA-induced innate immune responses to levels
508 similar to those of a MERS-CoV mutant lacking two accessory proteins that antagonize these
509 pathways, which highlights the distinctions among coronaviruses in interacting with these
510 pathways. However, like MERS-CoV and MHV, SARS-CoV-2 induces limited and late IFN/ISG
511 responses, indicating that proteins antagonizing innate immune responses are likely encoded.
512 Our future studies will focus on identifying specific innate immunity antagonists among lineage b
513 betacoronavirus accessory proteins as well as conserved nsp proteins. The recent development
514 of reverse genetics systems for SARS-CoV-2 (Hou et al., 2020; Thi Nhu Thao et al., 2020; Xie et
515 al., 2020) will allow us to study these proteins during viral infection. This will provide a system
516 complete with coronavirus-mediated alterations of cellular architecture typically nonexistent in

517 overexpression systems, which is critical to fully appreciate the functions of these proteins
518 (Knoops et al., 2008; Lundin et al., 2014; Sola et al., 2015). Our future studies will reveal key
519 features of SARS-CoV-2 biology, as well as those of other currently circulating SARS-related
520 viruses with pandemic potential.
521
522 **Materials and Methods**
523 **Viruses.** SARS-CoV-2 (USA-WA1/2020 strain) was obtained from BEI and propagated in Vero-
524 E6 cells. The genome RNA was sequenced was found to be identical to GenBank: MN985325.1**.**
525 Recombinant MERS-CoV and MERS-CoV-ΔNS4ab were described previously (Comar et al.,
526 2019) and were propagated in Vero-CCL81 cells. Sindbis virus Girdwood (G100) was obtained
527 from Dr. Mark Heise, University of North Carolina, Chapel Hill, and was prepared as previously
528 described (Suthar et al., 2005). Sendai virus (SeV) strain Cantell (Basler et al., 2003) was
529 obtained from Dr. Carolina B. Lopez (University of Pennsylvania).
530
531 **Cell lines**. African green monkey kidney Vero cells (E6) or (CCL81) (obtained from ATCC) were
532 cultured in Dulbecco's modified Eagle's medium (DMEM; Gibco catalog no. 11965),
533 supplemented with 10% fetal bovine serum (FBS), 100 U/ml of penicillin, 100 µg/ml streptomycin,
534 50 µg/ml gentamicin, 1mM sodium pyruvate, and 10mM HEPES. Human A549 cells(Verified by
535 ATCC) were cultured in RPMI 1640 (Gibco catalog no. 11875) supplemented with 10% FBS, 100
536 U/ml of penicillin, and 100 µg/ml streptomycin. Human HEK 293T cells were cultured in DMEM
537 supplemented with 10% FBS and 1 mM sodium pyruvate. Human Calu-3 cells (clone HTB-55)
538 were cultured in MEM supplemented with 20% FBS without antibiotics.
539
540
541 **Primary cell cultures**
542

543 **Human sinonasal air liquid interface (ALI) cultures.** Sinonasal mucosal specimens were
544 acquired from residual clinical material obtained during sinonasal surgery subsequent to approval
545 fromm The University of Pennsylvania Institutional Review Board. ALI cultures were established
546 from enzymatically dissociated human sinonasal epithelial cells (HSEC) as previously described
547 (Lee et al., 2017; Lee et al., 2014) and grown to confluence with bronchial epithelial basal medium
548 (BEBM; Lonza, Alpharetta, GA) supplemented with BEGM Singlequots (Lonza), 100 U/ml
549 penicillin and 0.25 µg /ml amphotericin B for 7 days. Cells were then trypsinized and seeded on
550 porous polyester membranes (2-3× $10^4$ cells per membrane) in cell culture inserts (Transwell-
551 clear, diameter 12 mm, 0.4 µm pores; Corning, Acton, MA). Five days later the culture medium
552 was removed from the upper compartment and the epithelium was allowed to differentiate by
553 using the differentiation medium consisting of 1:1 DMEM (Invitrogen, Grand Island, NY) and
554 BEBM (Lonza), supplemented with BEGM Singlequots (Lonza) with 0.1 nM retinoic acid (Sigma-
555 Aldrich), 100 UI/ml penicillin, 0.25 µg /ml amphotericin B and 2% Nu serum (Corning) in the basal
556 compartment. Cultures were fed every three days for 6 weeks prior to infection with SARS-CoV-
557 2. The day prior infection, the cells were fed and the apical side of the cultures were washed with
558 100µl of warm PBS X 3.
559
560 **Alveolar organoids and 2D cultures**. iPSC (SPC2 iPSC line, clone SPC2-ST-B2, Boston
561 University) derived alveolar epithelial type 2 cells (iAT2s) were differentiated and maintained as
562 alveolospheres embedded in 3D Matrigel in CK+DCI media, as previously described (Jacob et
563 al., 2019). iAT2s were passaged approximately every two weeks by dissociation into single cells
564 via the sequential application of dispase (2mg/ml, Thermo Fisher Scientific, 17105-04) for 1h at
565 37°C and 0.05% trypsin (Invitrogen, 25300054) for 15min at 37°C and re-plated at a density of
566 400 cells/µl of Matrigel (Corning, 356231) in CK+DCI media supplemented with ROCK inhibitor
567 for the first 48h, as previously described (Jacob et al., 2019). For generation of 2D alveolar cells
568 for viral infection, alveolospheres were dispersed into single cells, then plated on pre-coated 1/30

569 Matrigel plates at a cell density of 125,000 cells/cm2 using CK+DCI media with ROCK inhibitor
570 for the first 48h and then the medium was changed to CK+DCI media at day 3 and infected with
571 SARS-CoV-2 virus.
572
573 **Cardiomyocytes**. Experiments involving the use of human iPSCs were approved by the
574 University of Pennsylvania Embryonic Stem Cell Research Oversight Committee. The iPSC line
575 (PENN123i-SV20) used for cardiomyocyte generation was derived by the UPenn iPSC core as
576 previously described (Pashos et al., 2017; Yang et al., 2015). This line has been deposited at the
577 WiCell repository (Wicell.org). iPSCs were maintained on Geltrex (Thermofisher Scientific)-
578 coated plates in iPS-Brew XF (Miltenyi Biotec) media at 37°C in 5% $CO_2$/5% $O_2$/90% air humidified
579 atmosphere. Cells were passaged every 5-7 days using Stem-MACS Passaging Solution
580 (Miltenyi Biotec). Differentiation of SV20 into cardiomyocytes (iCMs) was performed using
581 previously described protocols (Laflamme et al., 2007; Palpant et al., 2017). In general, iCMs
582 were >95% positive for cardiac Troponin T staining by FACS. Day 18-25 differentiated cells were
583 replated and used for viral infection experiments.
584
585 **Generation of A549$^{ACE2}$ cells.** A549$^{ACE2}$ cells were constructed by lentivirus transduction of
586 *hACE2*. The plasmid encoding the cDNA of *hACE2* was purchased from Addgene. The cDNA
587 was amplified using forward primer 5′-ACTCTAGAATGTCAAGCTCTTCCTGGCTCCTTC-3′ and
588 reverse primer 5′-
589 TTGTCGACTTACGTAGAATCGAGACCGAGGAGAGGGTTAGGGATAGGCTTACCAAAGGAG
590 GTCTGAAC ′-3(Contained V5 tag sequences). The fragment containing hACE2-V5 was digested
591 by the XbaI and SalI restriction enzymes from the hACE2 cDNA and was cloned into pLenti-GFP
592 (Addgene) in place of green fluorescent protein (GFP), generating pLenti-hACE2-V5. The
593 resulting plasmids were packaged in lentiviruses pseudotyped with vesicular stomatitis virus
594 glycoprotein G (VSV-G) to establish the gene knock-in cells. Supernatants harvested 48 hours

595 post-transfection were used for transduction into A549 cells. Forty-eight hours after transduction,
596 cells were subjected to hygromycin (1 mg/ml) selection for 3 days and single-cell cloned. Clones
597 were screened for ACE2 expression and susceptibility to SARS-CoV-2 replication.
598
599 **CRISPR/Cas9 engineered cells**. *RNASEL*, *PKR* and *MAVS* KO A549$^{ACE2}$ cells were constructed
600 using the same Lenti-CRISPR system and guide RNA sequences as previously described (Li et
601 al., 2017; Li et al., 2016).
602 **Viral growth kinetics**. The nasal ALI cultures were apically infected with SARS-CoV-2(MOI=5),
603 MERS-CoV(MOI=5)**.** Briefly, viral stocks were diluted in nasal cell media, 50μl was added to each
604 well, the cells were incubated in 37°C for one hour, then the virus was removed and the cells were
605 wash three times with 200μl of PBS. For viral growth curves, at indicated time points, 200 μl of
606 PBS was added to the apical surface, collected 5 minutes later and frozen for subsequent analysis
607 of shed virus by plaque assay. The inserts were transferred to new 24-well plates with fresh media
608 after each collection. For iAT2 or iCM, cells were plated in 12 or 6-well plates, $4X10^5$ cells (iAT2)
609 or $6.25X10^5$ cells per well (iCM), cells were infected with SARS-CoV-2 at MOI=5 (iAT2) or
610 MOI=1(iCM). At 6, 24, 48 hours postinfection, 200μl of supernatant were harvested and stored
611 in -80°C for infectious virus titration. For infections, Cell lines were plated in 12-well plates, A549
612 and Vero-E6 at $5X10^5$ cells per well) and Calu-3 at $3X10^5$ cells per well). Viruses were diluted in
613 serum-free RPMI (A549 infections) or serum-free DMEM (Vero infections) or serum-free MEM
614 (Calu-3 infections) and added to cells for absorption for 1 hour at 37°C. Cells were washed three
615 times with PBS and fed with DMEM or RPMI +2% FBS for Vero and RPMI infections, respectively,
616 or 4% FBS in MEM for Calu-3 infections (Thornbrough et al., 2016). For virus titration 200 μl of
617 supernatant was collected at the times indicated and stored at -80°C for plaque assay on Vero-
618 E6 (SARS-CoV-2) or Vero-CCL81 (MERS-CoV) cells as previously described (Scobey et al.,
619 2013).

620

621 **Plaque assay.** Briefly virus supernatant was 10-fold serial diluted and inoculum was absorbed on
622 Vero cells for 1 hour at 37°C. Inoculum was overlaid with DMEM plus agarose (either 0.7% or
623 0.1%) and incubated for 3 days at 37°C. Cells were fixed with 4% paraformaldehyde and stained
624 with 1% crystal violet for counting plaques. All infections and virus manipulations were conducted
625 in a biosafety level 3 (BSL-3) laboratory using appropriate and approved personal protective
626 equipment and protocols.

627

628 **Immunofluorescent staining.** For nasal ALI culture, following 48 hours of infection, the cultures
629 were fixed in 4% paraformaldehyde at room temperature for 30 minutes. The transwell supports
630 were washed 3 times with PBS prior to excision of the membrane containing the cells. The cells
631 were permeabilized with 0.2% Triton X-100 in PBS and then immersed in PBS with 0.2% Triton
632 X-100, 10% normal donkey serum, and 1% BSA for 60 min at room temperature. Primary
633 antibody incubation was incubated overnight at 4 ºC (Type IV tubulin, Abcam ab11315, rabbit anti
634 SARS-CoV-2 Nucleocapsid protein, GeneTex, Irvine, CA). Visualization was carried out with Alex
635 Fluor®-conjugated donkey anti-mouse or anti-rabbit IgGs(Thermo-Fisher) (1:1000; 60 min
636 incubation at room temperature). Confocal images were acquired with an Olympus Fluoview
637 System (Z-axis step 0.5µm; sequential scanning). For iAT2, the cell monolayer was fixed using
638 4% paraformaldehyde (PFA) for 30min, 1X PBS was used to removed PFA and proceed with
639 antibody staining. Fixed cells were treated with a blocking solution containing 0.1% Triton X-100
640 and 5% donkey serum in 1X PBS for 30min. Immunostaining was performed for SARS-CoV-2
641 nucleocapsid protein expression using the SARS-CoV-2 nucleocapsid antibody at 1:1000 dilution
642 in blocking solution incubated for 30min. After washing primary antibody away, a secondary Alexa
643 fluor 488 donkey anti-rabbit IgG(H+L) antibody(Thermo-Fisher) was used at 1:400 dilution in
644 blocking solution and incubated for 30min. Secondary antibody was washed away with 1X PBS

645 and DAPI was used for nuclear staining at 2.5μg/ml. iCM were fixed in 4% paraformaldehyde and
646 permeabilized with 0.1% Triton X-100 for 15min. Cells were blocked with 10% normal donkey
647 serum (Sigma D9663) in 0.2% Tween 20 (Biorad 170-6531) for 1hr. Antibodies against cardiac
648 troponin T (cTnT, Abcam ab8295; 1:100 mouse) and SARS-CoV-2 nucleocapsid were incubated
649 with cells in blocking solution overnight at 4 °C. Donkey anti-mouse Alexa Fluor 647 (Invitrogen
650 A31571) and Donkey anti-rabbit Alexa Fluor 488 (Invitrogen A21206) were diluted 1:250 in
651 blocking solution and incubated with cells for 2hr at RT. Slides were mounted in Slowfade Gold
652 anti-fade reagent with DAPI (Invitrogen S36939). Images were acquired with BZ-X710 all-in-one
653 fluorescence microscope equipped with BZ-X Viewer software (Keyence Corporation). At the
654 indicated times post-infection cells were fixed onto glass coverslips (Calu-3 coverslips were
655 coated with rat tail collagen type-1: Cell Applications, Inc. Cat. # 122-20) with 4%
656 paraformaldehyde for 30 minutes at room temperature. Cells were then washed three times with
657 PBS and permeabilized for 10 minutes with PBS+0.1% Triton-X100. Cells were then blocked in
658 PBS and 3% BSA for 30-60 minutes at room temperature. Primary antibodies were diluted in
659 block buffer and incubated on a rocker at room temperature for one hour. Cells were washed
660 three times with block buffer and then incubated rocking at room temperature for 60 minutes with
661 secondary antibodies diluted in block buffer. Finally, cells were washed twice with block buffer
662 and once with PBS, and nuclei stained with DAPI diluted in PBS (2ng/uL final concentration).
663 SARS-CoV-2 nucleoprotein and dsRNA (J2,1:1000, Scions) were detected. Secondary
664 antibodies were from Invitrogen: goat anti-mouse IgG AlexaFluor594 (A-11005) for J2 and goat
665 anti-rabbit IgG AlexaFluor488 (A-11070) for nucleocapsid. Coverslips were mounted onto slides
666 for analysis by widefield microscopy with Nikon Eclipse Ti2 using a Nikon 40x/0.95NA Plan APO
667 objective and NikonDS-Qi1Mc-U3 12 bit camera. Images were processed using Fiji/Image J
668 software.
669

670 **Western immunoblotting.** Cells were washed once with ice-cold PBS and lysates harvested at
671 the indicated times post infection with lysis buffer (1% NP40, 2mM EDTA, 10% glycerol, 150mM
672 NaCl, 50mM Tris HCl) supplemented with protease inhibitors (Roche – complete mini EDTA-free
673 protease inhibitor) and phosphatase inhibitors (Roche – PhosStop easy pack). After 5 minutes
674 lysates were harvested, incubated on ice for 20 minutes, centrifuged for 20 minutes at 4°C and
675 supernatants mixed 3:1 with 4x Laemmli sample buffer. Samples were heated at 95°C for 5
676 minutes, then separated on 4-15% SDS-PAGE, and transferred to polyvinylidene difluoride
677 (PVDF) membranes. Blots were blocked with 5% nonfat milk or 5% BSA and probed with
678 antibodies (table below) diluted in the same block buffer. Primary antibodies were incubated
679 overnight at 4°C or for 1 hour at room temperature. All secondary antibody incubation steps were
680 done for 1 hour at room temperature. Blots were visualized using Thermo Scientific SuperSignal
681 west chemiluminescent substrates (Cat #: 34095 or 34080). Blots were probed sequentially with
682 antibodies and in between antibody treatments stripped using Thermo scientific Restore western
683 blot stripping buffer (Cat #: 21059).
684
685

| **Primary Antibody** | **Antibody species** | **Blocking buffer** | **Dilution** | **Catalog number** |
|---|---|---|---|---|
| p-PKR (phospho-T446) [E120] | rabbit | 5% milk/TBST | 1 : 1000 | Abcam 32036 |
| PKR (D7F7) | rabbit | 5% milk/TBST | 1:1000 | Cell Signaling Technology 12297S |
| p-eif2α (S51) | rabbit | 5% BSA/TBST | 1:1000 | Cell Signaling Technology 9721S |
| eif2α | rabbit | 5% BSA/TBST | 1:1000 | Cell Signaling Technology 9722S |
| GAPDH (14C10) | rabbit | 5% milk/TBST | 1:2000 | Cell Signaling Technology 2118S |
| SARS-CoV-2 N | rabbit | 5% milk/TBST | 1:2000 | GTX135357 (Gentex) |
| MERS-CoV N | mouse | 5% milk/TBST | 1:2000 | 40068-MM10 (Sino Biological) |
| pSTAT1 (Tyr701) | rabbit | 5% BSA/TBST | 1:1000 | Cell Signaling Technology 7649 |

| | | | | |
|---|---|---|---|---|
| STAT1 | mouse | 5% BSA/TBST | 1:1000 | Santa Cruz (C136): SC-464 |
| ACE2 | rabbit | 5% milk/TBST | 1:1000 | Cell Signaling Technology 4355S |
| MAVS | rabbit | 5% milk/TBST | 1:1000 | Cell Signaling Technology 24930S |
| V5 | rabbit | 5% milk/TBST | 1:1000 | Cell Signaling Technology 13202S |
| RNase L | mouse | 5% milk/TBST | 1:1000 | gift from Dr. Robert Silverman (Cleveland Clinic) |
| MDA5 | rabbit | 5% milk/TBST | 1:1000 | Cell Signaling Technology 5321S |
| **Secondary Antibody** | | | | |
| goat anti-rabbit IgG | HRP linked | same as primary | 1:3000 | Cell Signaling Technology 7074S |
| goat anti-mouse IgG | HRP linked | same as primary | 1:3000 | Cell Signaling Technology 7076S |

686

687 **Quantitative PCR (RT-qPCR).**

688 A549, Calu-3, and iAT2 cells were lysed at indicated times post infection in RLT buffer and DNase-
689 treated before total RNA was extracted using the RNeasy Plus Mini Kit (Qiagen). RNA from iCM
690 and nasal cells was extracted using TRIzol-LS (Ambion), and DNase-treated using the DNA-
691 *free*™ Kit (Invitrogen). RNA was reverse transcribed into cDNA with a High Capacity cDNA
692 Reverse Transcriptase Kit (Applied Biosystems). cDNA was amplified using specific RT-qPCR
693 primers (see Table below), iQ™ SYBR® Green Supermix (Bio-Rad), and the QuantStudio™ 3
694 PCR system (Thermo Fisher). Host gene expression displayed as fold change over mock-infected
695 samples was generated by first normalizing cycle threshold ($C_T$) values to 18S rRNA to generate
696 $\Delta C_T$ values ($\Delta C_T$ = $C_T$ gene of interest - $C_T$ 18S rRNA). Next, $\Delta(\Delta C_T)$ values were determined by
697 subtracting the mock-infected $\Delta C_T$ values from the virus-infected samples. Technical triplicates
698 were averaged and means displayed using the equation $2^{-\Delta(\Delta CT)}$. For basal expression levels, $C_T$
699 values were normalized to 18S rRNA to generate $\Delta C_T$ values ($\Delta C_T$ = $C_T$ gene of interest - $C_T$ 18S
700 rRNA), and displayed as $2^{-\Delta Ct}$. Basal expression levels were also calculated as fold change over
701 $A549^{ACE2}$ clone 44 using the equation $2^{-\Delta(\Delta CT)}$. $\Delta(\Delta C_T)$ values were calculated by subtracting $\Delta C_T$

702 values from each cell type from the $\Delta C_T$ value of $A549^{ACE2}$ clone 44. Absolute quantification of
703 SARS-CoV-2 and MERS-CoV genomes was calculated using a standard curve generated from
704 serially diluted known concentrations of a digested plasmid containing the region of interest. For
705 SARS-CoV-2, construct pcDNA6B-nCoV-NSP12-FLAG encoding the RDRP gene (gift from Dr.
706 George Stark, Cleveland Clinic) was digested with Xho1 and purified by Qiagen QIAquick PCR
707 Purification Kit to be used as a standard in the RT-qPCR reaction. For MERS-CoV, cDNA MERS-
708 D1 (Scobey et al., 2013) containing basepairs 12259–15470 of the MERS-CoV genome was
709 digested with BglI and purified by Qiagen QIAquick PCR Purification Kit to be used as a standard
710 in the RT-PCR reaction. Copy numbers were generated by standard curve analysis in the
711 QuantStudio™ 3 software, and copy numbers per ug RNA were calculated based on the volume
712 of cDNA used in the qPCR reaction, and concentration of RNA used to generated cDNA. Primer
713 sequences are as follows:
714

| | Forward primer (5' to 3') | Reverse primer (5' to 3') |
|---|---|---|
| *IFNL1* | CGCCTTGGAAGAGTCACTCA | GAAGCCTCAGGTCCCAATTC |
| *OAS2* | TTCTGCCTGCACCACTCTTCACGAC | GCCAGTCTTCAGAGCTGTGCCTTTG |
| *IFIT1* | 5'-TGGTGACCTGGGGCAACTTT | AGGCCTTGGCCCGTTCATAA |
| *IFNB* | GTCAGAGTGGAAATCCTAAG | ACAGCATCTGCTGGTTGAAG |
| GAPDH | GCAAATTCCATGGCACCGT | TCGCCCCACTTGATTTTGG |
| *IFIH1* | GCACAGAGCGGTAGACCCTGCTT | AGGCCTTGGCCCGTTCATAA |
| *CXCL8* | GAGAGTGATTGAGAGTGGACCAC | CACAACCCTCTGCACCCAGTTT |
| 18S rRNA | TTCGATGGTAGTCGCTGTGC | CTGCTGCCTTCCTTGAATGTGGTA |
| SARS-CoV-2 genome (nsp12/RdRp) | GGTAACTGGTATGATTTCG | CTGGTCAAGGTTAATATAGG |

| | | |
|---|---|---|
| MERS-CoV genome (nsp7) | GCACATCTGTGGTTCTCCTCTCT | AAGCCCAGGCCCTACTATTAGC |

715

716

717 **Analyses of RNase L-mediated rRNA degradation.** RNA was harvested with buffer RLT
718 (Qiagen RNeasy #74106) or Trizol-LS (Ambion) and analyzed on an RNA chip with an Agilent
719 Bioanalyzer using the Agilent RNA 6000 Nano Kit and its prescribed protocol as we have
720 described previously (Cat #: 5067-1511).

721

722 **Statistical analysis.** All statistical analyses and plotting of data were performed using GraphPad
723 Prism software (GraphPad Software, Inc., CA). SARS-CoV-2 and MERS-CoV replication trends
724 in nasal cells were analyzed by two-way ANOVA comparing averaged titers from all four donor
725 cells for each virus at each timepoint. MERS-CoV and MERS-CoV-ΔNS4ab viral replication and
726 primary cell RT-qPCR gene expression between SARS-CoV-2 and SINV were analyzed by paired
727 Student *t* test. RT-qPCR analysis in $A549^{ACE2}$ cells was analyzed by one-way ANOVA, comparing
728 SARS-CoV-2 at each timepoint to SINV. RT-qPCR analysis in Calu-3 cells was analyzed by two-
729 way ANOVA, comparing SARS-CoV-2 at each timepoint to MERS-CoV and MERS-CoV-ΔNS4ab.
730 SARS-CoV-2 replication in $A549^{ACE2}$ WT cells compared with $A549^{ACE2}$ KO cells was analyzed by
731 two-way ANOVA. Displayed significance is determined by p-value (P), where * = $P < 0.05$; ** = P
732 $< 0.01$; *** = $P < 0.001$; **** = $P < 0.0001$; ns = not significant.

733

734

735 **Acknowledgements**

736 We thank Nicholas Parenti for technical help and Dr. Nikki Tanneti for reading the manuscript.
737 This work was supported by NIH grants AI140442 and supplement for SARS-CoV-2 (SRW),
738 AI104887 (SRW and RHS); funds from Penn Center for Coronavirus Research and Other

739 Emerging Pathogens (SRW, YL); NIH grants U01HL148857, R01HL087825, U01HL134745 and
740 R01HL132999 (EM); VA administration grant CX001617 (NAC); NIH grants U01TR001810, N01
741 75N92020C00005, R01HL095993, and an Evergrande MassCPR award (DNK, JH, and KDA).
742 RT and WY were supported in part by institutional funds from the University of Pennsylania
743 Perelman School of Medicine to the iPSC Core and by NIH grant U01TR001810. DMR was
744 supported in part by T32-AI055400 and CEC was supported in part by T32 NS-007180,

745

746 **Author Contributions**

747 Conceptualization: YL, CEC, DMR, SRW
748 Methodology: YL CEC, DMR, JNW, HMR, WY, NAC, JNP, NDA, MAK, EM, RHS, SRW.
749 Investigation, Performed experiments: YL, CEC, DMR, JNW, HMR, FLC-D, RT, LHT, BD
750 Writing –Original Draft: SRW, JNW
751 Writing –Review & Editing: YL, CEC, DMR, JNW, HMR, SRW, EM, NAC, WY, DNK
752 Funding Acquisition: SRW, WY, EM, NC, RHS, DNK
753 Resources: WY, NC, EM, RHS, SRW
754 Supervision: WY, NC, EM, RHS, SRW

755 **Declaration of Interests**

756 The authors declare no competing interests.

757

758

759 **References**

760 Ank, N., Iversen, M.B., Bartholdy, C., Staeheli, P., Hartmann, R., Jensen, U.B., Dagnaes-Hansen,
761 F., Thomsen, A.R., Chen, Z., Haugen, H.*, et al.* (2008). An important role for type III interferon
762 (IFN-lambda/IL-28) in TLR-induced antiviral activity. J Immunol *180*, 2474-2485.
763
764 Arabi, Y.M., Balkhy, H.H., Hayden, F.G., Bouchama, A., Luke, T., Baillie, J.K., Al-Omari, A., Hajeer,
765 A.H., Senga, M., Denison, M.R.*, et al.* (2017). Middle East Respiratory Syndrome. N Engl J Med
766 *376*, 584-594.
767
768 Banerjee, S., Chakrabarti, A., Jha, B.K., Weiss, S.R., and Silverman, R.H. (2014). Cell-type-specific
769 effects of RNase L on viral induction of beta interferon. mBio *5*, e00856-00814.
770
771 Basler, C.F., Mikulasova, A., Martinez-Sobrido, L., Paragas, J., Muhlberger, E., Bray, M., Klenk,
772 H.D., Palese, P., and Garcia-Sastre, A. (2003). The Ebola virus VP35 protein inhibits activation of
773 interferon regulatory factor 3. Journal of virology *77*, 7945-7956.

774
775 Belouzard, S., Chu, V.C., and Whittaker, G.R. (2009). Activation of the SARS coronavirus spike
776 protein via sequential proteolytic cleavage at two distinct sites. Proceedings of the National
777 Academy of Sciences of the United States of America *106*, 5871-5876.
778
779 Bender, S.J., Phillips, J.M., Scott, E.P., and Weiss, S.R. (2010). Murine coronavirus receptors are
780 differentially expressed in the central nervous system and play virus strain-dependent roles in
781 neuronal spread. Journal of virology *84*, 11030-11044.
782
783 Birdwell, L.D., Zalinger, Z.B., Li, Y., Wright, P.W., Elliott, R., Rose, K.M., Silverman, R.H., and
784 Weiss, S.R. (2016). Activation of RNase L by murine coronavirus in myeloid cells is dependent on
785 basal Oas gene expression and independent of virus-induced interferon. Journal of virology.
786
787 Blanco-Melo, D., Nilsson-Payant, B.E., Liu, W.C., Uhl, S., Hoagland, D., Moller, R., Jordan, T.X.,
788 Oishi, K., Panis, M., Sachs, D*., et al.* (2020). Imbalanced Host Response to SARS-CoV-2 Drives
789 Development of COVID-19. Cell *181*, 1036-1045 e1039.
790
791 Boni, M.F., Lemey, P., Jiang, X., Lam, T.T., Perry, B.W., Castoe, T.A., Rambaut, A., and Robertson,
792 D.L. (2020). Evolutionary origins of the SARS-CoV-2 sarbecovirus lineage responsible for the
793 COVID-19 pandemic. Nat Microbiol.
794
795 Canton, J., Fehr, A.R., Fernandez-Delgado, R., Gutierrez-Alvarez, F.J., Sanchez-Aparicio, M.T.,
796 Garcia-Sastre, A., Perlman, S., Enjuanes, L., and Sola, I. (2018). MERS-CoV 4b protein interferes
797 with the NF-kappaB-dependent innate immune response during infection. PLoS pathogens *14*,
798 e1006838.
799
800 Castelli, J.C., Hassel, B.A., Wood, K.A., Li, X.L., Amemiya, K., Dalakas, M.C., Torrence, P.F., and
801 Youle, R.J. (1997). A study of the interferon antiviral mechanism: apoptosis activation by the 2-
802 5A system. The Journal of experimental medicine *186*, 967-972.
803
804 Chakrabarti, A., Banerjee, S., Franchi, L., Loo, Y.M., Gale, M., Jr., Nunez, G., and Silverman, R.H.
805 (2015). RNase L activates the NLRP3 inflammasome during viral infections. Cell host & microbe
806 *17*, 466-477.
807
808 Channappanavar, R., Fehr, A.R., Vijay, R., Mack, M., Zhao, J., Meyerholz, D.K., and Perlman, S.
809 (2016). Dysregulated Type I Interferon and Inflammatory Monocyte-Macrophage Responses
810 Cause Lethal Pneumonia in SARS-CoV-Infected Mice. Cell host & microbe *19*, 181-193.
811
812 Channappanavar, R., Fehr, A.R., Zheng, J., Wohlford-Lenane, C., Abrahante, J.E., Mack, M.,
813 Sompallae, R., McCray, P.B., Jr., Meyerholz, D.K., and Perlman, S. (2019). IFN-I response timing
814 relative to virus replication determines MERS coronavirus infection outcomes. The Journal of
815 clinical investigation *129*, 3625-3639.
816

817 Channappanavar, R., and Perlman, S. (2017). Pathogenic human coronavirus infections: causes
818 and consequences of cytokine storm and immunopathology. Semin Immunopathol *39*, 529-539.
819
820 Comar, C.E., Goldstein, S.A., Li, Y., Yount, B., Baric, R.S., and Weiss, S.R. (2019). Antagonism of
821 dsRNA-Induced Innate Immune Pathways by NS4a and NS4b Accessory Proteins during MERS
822 Coronavirus Infection. mBio *10*.
823
824 Cruz, J.L., Sola, I., Becares, M., Alberca, B., Plana, J., Enjuanes, L., and Zuniga, S. (2011).
825 Coronavirus gene 7 counteracts host defenses and modulates virus virulence. PLoS pathogens
826 *7*, e1002090.
827
828 Cui, J., Li, F., and Shi, Z.L. (2019). Origin and evolution of pathogenic coronaviruses. Nature
829 reviews Microbiology *17*, 181-192.
830
831 de Haan, C.A., Stadler, K., Godeke, G.J., Bosch, B.J., and Rottier, P.J. (2004). Cleavage inhibition
832 of the murine coronavirus spike protein by a furin-like enzyme affects cell-cell but not virus-cell
833 fusion. Journal of virology *78*, 6048-6054.
834
835 Dedeurwaerder, A., Olyslaegers, D.A., Desmarets, L.M., Roukaerts, I.D., Theuns, S., and
836 Nauwynck, H.J. (2014). ORF7-encoded accessory protein 7a of feline infectious peritonitis virus
837 as a counteragent against IFN-alpha-induced antiviral response. The Journal of general virology
838 *95*, 393-402.
839
840 Deng, X., Hackbart, M., Mettelman, R.C., O'Brien, A., Mielech, A.M., Yi, G., Kao, C.C., and Baker,
841 S.C. (2017). Coronavirus nonstructural protein 15 mediates evasion of dsRNA sensors and limits
842 apoptosis in macrophages. Proceedings of the National Academy of Sciences of the United
843 States of America *114*, E4251-E4260.
844
845 Fehr, A.R., and Perlman, S. (2015). Coronaviruses: an overview of their replication and
846 pathogenesis. Methods Mol Biol *1282*, 1-23.
847
848 Forero, A., Ozarkar, S., Li, H., Lee, C.H., Hemann, E.A., Nadjsombati, M.S., Hendricks, M.R., So,
849 L., Green, R., Roy, C.N.*, et al.* (2019). Differential Activation of the Transcription Factor IRF1
850 Underlies the Distinct Immune Responses Elicited by Type I and Type III Interferons. Immunity
851 *51*, 451-464 e456.
852
853 Frieman, M., Yount, B., Heise, M., Kopecky-Bromberg, S.A., Palese, P., and Baric, R.S. (2007).
854 Severe acute respiratory syndrome coronavirus ORF6 antagonizes STAT1 function by
855 sequestering nuclear import factors on the rough endoplasmic reticulum/Golgi membrane.
856 Journal of virology *81*, 9812-9824.
857
858 Galani, I.E., Triantafyllia, V., Eleminiadou, E.E., Koltsida, O., Stavropoulos, A., Manioudaki, M.,
859 Thanos, D., Doyle, S.E., Kotenko, S.V., Thanopoulou, K.*, et al.* (2017). Interferon-lambda

860 Mediates Non-redundant Front-Line Antiviral Protection against Influenza Virus Infection
861 without Compromising Host Fitness. Immunity *46*, 875-890 e876.
862
863 Giamarellos-Bourboulis, E.J., Netea, M.G., Rovina, N., Akinosoglou, K., Antoniadou, A.,
864 Antonakos, N., Damoraki, G., Gkavogianni, T., Adami, M.E., Katsaounou, P.*, et al.* (2020).
865 Complex Immune Dysregulation in COVID-19 Patients with Severe Respiratory Failure. Cell host
866 & microbe *27*, 992-1000 e1003.
867
868 Gombold, J.L., Hingley, S.T., and Weiss, S.R. (1993). Fusion-defective mutants of mouse
869 hepatitis virus A59 contain a mutation in the spike protein cleavage signal. Journal of virology
870 *67*, 4504-4512.
871
872 Gordon, D.E., Jang, G.M., Bouhaddou, M., Xu, J., Obernier, K., White, K.M., O'Meara, M.J.,
873 Rezelj, V.V., Guo, J.Z., Swaney, D.L.*, et al.* (2020). A SARS-CoV-2 protein interaction map reveals
874 targets for drug repurposing. Nature *583*, 459-468.
875
876 Hadjadj, J., Yatim, N., Barnabei, L., Corneau, A., Boussier, J., Smith, N., Pere, H., Charbit, B.,
877 Bondet, V., Chenevier-Gobeaux, C.*, et al.* (2020). Impaired type I interferon activity and
878 inflammatory responses in severe COVID-19 patients. Science.
879
880 Hou, Y.J., Okuda, K., Edwards, C.E., Martinez, D.R., Asakura, T., Dinnon, K.H., 3rd, Kato, T., Lee,
881 R.E., Yount, B.L., Mascenik, T.M.*, et al.* (2020). SARS-CoV-2 Reverse Genetics Reveals a Variable
882 Infection Gradient in the Respiratory Tract. Cell *182*, 429-446 e414.
883
884 Hur, S. (2019). Double-Stranded RNA Sensors and Modulators in Innate Immunity. Annu Rev
885 Immunol *37*, 349-375.
886
887 Jacob, A., Vedaie, M., Roberts, D.A., Thomas, D.C., Villacorta-Martin, C., Alysandratos, K.D.,
888 Hawkins, F., and Kotton, D.N. (2019). Derivation of self-renewing lung alveolar epithelial type II
889 cells from human pluripotent stem cells. Nature protocols *14*, 3303-3332.
890
891 Kang, R., and Tang, D. (2012). PKR-dependent inflammatory signals. Science signaling *5*, pe47.
892
893 Kikkert, M. (2020). Innate Immune Evasion by Human Respiratory RNA Viruses. J Innate Immun
894 *12*, 4-20.
895
896 Kindler, E., Gil-Cruz, C., Spanier, J., Li, Y., Wilhelm, J., Rabouw, H.H., Zust, R., Hwang, M.,
897 V'Kovski, P., Stalder, H.*, et al.* (2017). Early endonuclease-mediated evasion of RNA sensing
898 ensures efficient coronavirus replication. PLoS pathogens *13*, e1006195.
899
900 Knoops, K., Kikkert, M., Worm, S.H., Zevenhoven-Dobbe, J.C., van der Meer, Y., Koster, A.J.,
901 Mommaas, A.M., and Snijder, E.J. (2008). SARS-coronavirus replication is supported by a
902 reticulovesicular network of modified endoplasmic reticulum. PLoS Biol *6*, e226.
903

904 Koetzner, C.A., Kuo, L., Goebel, S.J., Dean, A.B., Parker, M.M., and Masters, P.S. (2010).
905 Accessory protein 5a is a major antagonist of the antiviral action of interferon against murine
906 coronavirus. Journal of virology *84*, 8262-8274.
907
908 Konno, Y., Kimura, I., Uriu, K., Fukushi, M., Irie, T., Koyanagi, Y., Nakagawa, S., and Sato, K.
909 (2020). SARS-CoV-2 ORF3b is a potent interferon antagonist whose activity is further increased
910 by a naturally occurring elongation variant. bioRxiv, 2020.2005.2011.088179.
911
912 Kopecky-Bromberg, S.A., Martinez-Sobrido, L., Frieman, M., Baric, R.A., and Palese, P. (2007).
913 Severe acute respiratory syndrome coronavirus open reading frame (ORF) 3b, ORF 6, and
914 nucleocapsid proteins function as interferon antagonists. Journal of virology *81*, 548-557.
915
916 Laflamme, M.A., Chen, K.Y., Naumova, A.V., Muskheli, V., Fugate, J.A., Dupras, S.K., Reinecke,
917 H., Xu, C., Hassanipour, M., Police, S.*, et al.* (2007). Cardiomyocytes derived from human
918 embryonic stem cells in pro-survival factors enhance function of infarcted rat hearts. Nat
919 Biotechnol *25*, 1015-1024.
920
921 Lee, R.J., Hariri, B.M., McMahon, D.B., Chen, B., Doghramji, L., Adappa, N.D., Palmer, J.N.,
922 Kennedy, D.W., Jiang, P., Margolskee, R.F.*, et al.* (2017). Bacterial d-amino acids suppress
923 sinonasal innate immunity through sweet taste receptors in solitary chemosensory cells.
924 Science signaling *10*.
925
926 Lee, R.J., Kofonow, J.M., Rosen, P.L., Siebert, A.P., Chen, B., Doghramji, L., Xiong, G., Adappa,
927 N.D., Palmer, J.N., Kennedy, D.W.*, et al.* (2014). Bitter and sweet taste receptors regulate
928 human upper respiratory innate immunity. The Journal of clinical investigation *124*, 1393-1405.
929
930 Li, Y., Banerjee, S., Goldstein, S.A., Dong, B., Gaughan, C., Rath, S., Donovan, J., Korennykh, A.,
931 Silverman, R.H., and Weiss, S.R. (2017). Ribonuclease L mediates the cell-lethal phenotype of
932 double-stranded RNA editing enzyme ADAR1 deficiency in a human cell line. eLife *6*.
933
934 Li, Y., Banerjee, S., Wang, Y., Goldstein, S.A., Dong, B., Gaughan, C., Silverman, R.H., and Weiss,
935 S.R. (2016). Activation of RNase L is dependent on OAS3 expression during infection with
936 diverse human viruses. Proceedings of the National Academy of Sciences of the United States of
937 America *113*, 2241-2246.
938
939 Li, Y., Dong, B., Wei, Z., Silverman, R.H., and Weiss, S.R. (2019). Activation of RNase L in Egyptian
940 Rousette Bat-Derived RoNi/7 Cells Is Dependent Primarily on OAS3 and Independent of MAVS
941 Signaling. mBio *10*.
942
943 Li, Y., and Weiss, S.R. (2016). Antagonism of RNase L Is Required for Murine Coronavirus
944 Replication in Kupffer Cells and Liver Sinusoidal Endothelial Cells but Not in Hepatocytes.
945 Journal of virology *90*, 9826-9832.
946

947 Lindner, D., Fitzek, A., Brauninger, H., Aleshcheva, G., Edler, C., Meissner, K., Scherschel, K.,
948 Kirchhof, P., Escher, F., Schultheiss, H.P.*, et al.* (2020). Association of Cardiac Infection With
949 SARS-CoV-2 in Confirmed COVID-19 Autopsy Cases. JAMA Cardiol.
950
951 Llanes, A., Restrepo, C.M., Caballero, Z., Rajeev, S., Kennedy, M.A., and Lleonart, R. (2020).
952 Betacoronavirus Genomes: How Genomic Information has been Used to Deal with Past
953 Outbreaks and the COVID-19 Pandemic. Int J Mol Sci *21*.
954
955 Lokugamage, K.G., Hage, A., de Vries, M., Valero-Jimenez, A.M., Schindewolf, C., Dittmann, M.,
956 Rajsbaum, R., and Menachery, V.D. (2020). Type I interferon susceptibility distinguishes SARS-
957 CoV-2 from SARS-CoV. Journal of virology.
958
959 Lopusna, K., Rezuchova, I., Betakova, T., Skovranova, L., Tomaskova, J., Lukacikova, L., and
960 Kabat, P. (2013). Interferons lambda, new cytokines with antiviral activity. Acta Virol *57*, 171-
961 179.
962
963 Lu, R., Zhao, X., Li, J., Niu, P., Yang, B., Wu, H., Wang, W., Song, H., Huang, B., Zhu, N.*, et al.*
964 (2020). Genomic characterisation and epidemiology of 2019 novel coronavirus: implications for
965 virus origins and receptor binding. Lancet *395*, 565-574.
966
967 Lundin, A., Dijkman, R., Bergstrom, T., Kann, N., Adamiak, B., Hannoun, C., Kindler, E.,
968 Jonsdottir, H.R., Muth, D., Kint, J.*, et al.* (2014). Targeting membrane-bound viral RNA synthesis
969 reveals potent inhibition of diverse coronaviruses including the middle East respiratory
970 syndrome virus. PLoS pathogens *10*, e1004166.
971
972 Malathi, K., Dong, B., Gale, M., Jr., and Silverman, R.H. (2007). Small self-RNA generated by
973 RNase L amplifies antiviral innate immunity. Nature *448*, 816-819.
974
975 Mukaida, N. (2003). Pathophysiological roles of interleukin-8/CXCL8 in pulmonary diseases.
976 American journal of physiology Lung cellular and molecular physiology *284*, L566-577.
977
978 Ng, D.L., Al Hosani, F., Keating, M.K., Gerber, S.I., Jones, T.L., Metcalfe, M.G., Tong, S., Tao, Y.,
979 Alami, N.N., Haynes, L.M.*, et al.* (2016). Clinicopathologic, Immunohistochemical, and
980 Ultrastructural Findings of a Fatal Case of Middle East Respiratory Syndrome Coronavirus
981 Infection in the United Arab Emirates, April 2014. Am J Pathol *186*, 652-658.
982
983 Oh, M.D., Park, W.B., Choe, P.G., Choi, S.J., Kim, J.I., Chae, J., Park, S.S., Kim, E.C., Oh, H.S., Kim,
984 E.J.*, et al.* (2016). Viral Load Kinetics of MERS Coronavirus Infection. N Engl J Med *375*, 1303-
985 1305.
986
987 Palpant, N.J., Pabon, L., Friedman, C.E., Roberts, M., Hadland, B., Zaunbrecher, R.J., Bernstein,
988 I., Zheng, Y., and Murry, C.E. (2017). Generating high-purity cardiac and endothelial derivatives
989 from patterned mesoderm using human pluripotent stem cells. Nature protocols *12*, 15-31.
990

991 Pashos, E.E., Park, Y., Wang, X., Raghavan, A., Yang, W.L., Abbey, D., Peters, D.T., Arbelaez, J.,
992 Hernandez, M., Kuperwasser, N.*, et al.* (2017). Large, Diverse Population Cohorts of hiPSCs and
993 Derived Hepatocyte-like Cells Reveal Functional Genetic Variation at Blood Lipid-Associated
994 Loci. Cell Stem Cell *20*, 558-+.
995
996 Perlman, S., and Netland, J. (2009). Coronaviruses post-SARS: update on replication and
997 pathogenesis. Nature reviews Microbiology *7*, 439-450.
998
999 Platanias, L.C. (2005). Mechanisms of type-I- and type-II-interferon-mediated signalling. Nature
1000 reviews Immunology *5*, 375-386.
1001
1002 Puelles, V.G., Lutgehetmann, M., Lindenmeyer, M.T., Sperhake, J.P., Wong, M.N., Allweiss, L.,
1003 Chilla, S., Heinemann, A., Wanner, N., Liu, S.*, et al.* (2020). Multiorgan and Renal Tropism of
1004 SARS-CoV-2. N Engl J Med *383*, 590-592.
1005
1006 Qian, Z., Travanty, E.A., Oko, L., Edeen, K., Berglund, A., Wang, J., Ito, Y., Holmes, K.V., and
1007 Mason, R.J. (2013). Innate immune response of human alveolar type II cells infected with severe
1008 acute respiratory syndrome-coronavirus. American journal of respiratory cell and molecular
1009 biology *48*, 742-748.
1010
1011 Qiu, Z., Hingley, S.T., Simmons, G., Yu, C., Das Sarma, J., Bates, P., and Weiss, S.R. (2006).
1012 Endosomal proteolysis by cathepsins is necessary for murine coronavirus mouse hepatitis virus
1013 type 2 spike-mediated entry. Journal of virology *80*, 5768-5776.
1014
1015 Rabouw, H.H., Langereis, M.A., Knaap, R.C., Dalebout, T.J., Canton, J., Sola, I., Enjuanes, L.,
1016 Bredenbeek, P.J., Kikkert, M., de Groot, R.J.*, et al.* (2016). Middle East Respiratory Coronavirus
1017 Accessory Protein 4a Inhibits PKR-Mediated Antiviral Stress Responses. PLoS pathogens *12*,
1018 e1005982.
1019
1020 Roth-Cross, J.K., Bender, S.J., and Weiss, S.R. (2008). Murine coronavirus mouse hepatitis virus
1021 is recognized by MDA5 and induces type I interferon in brain macrophages/microglia. Journal of
1022 virology *82*, 9829-9838.
1023
1024 Sadler, A.J., and Williams, B.R. (2008). Interferon-inducible antiviral effectors. Nature reviews
1025 Immunology *8*, 559-568.
1026
1027 Sanche, S., Lin, Y.T., Xu, C., Romero-Severson, E., Hengartner, N., and Ke, R. (2020). High
1028 Contagiousness and Rapid Spread of Severe Acute Respiratory Syndrome Coronavirus 2.
1029 Emerging infectious diseases *26*, 1470-1477.
1030
1031 Scobey, T., Yount, B.L., Sims, A.C., Donaldson, E.F., Agnihothram, S.S., Menachery, V.D.,
1032 Graham, R.L., Swanstrom, J., Bove, P.F., Kim, J.D.*, et al.* (2013). Reverse genetics with a full-
1033 length infectious cDNA of the Middle East respiratory syndrome coronavirus. Proceedings of
1034 the National Academy of Sciences of the United States of America *110*, 16157-16162.

1035
1036 Sharma, A., Garcia, G., Jr., Wang, Y., Plummer, J.T., Morizono, K., Arumugaswami, V., and
1037 Svendsen, C.N. (2020). Human iPSC-Derived Cardiomyocytes Are Susceptible to SARS-CoV-2
1038 Infection. Cell Rep Med *1*, 100052.
1039
1040 Shi, S., Qin, M., Shen, B., Cai, Y., Liu, T., Yang, F., Gong, W., Liu, X., Liang, J., Zhao, Q.*, et al.*
1041 (2020). Association of Cardiac Injury With Mortality in Hospitalized Patients With COVID-19 in
1042 Wuhan, China. JAMA Cardiol.
1043
1044 Sims, A.C., Tilton, S.C., Menachery, V.D., Gralinski, L.E., Schafer, A., Matzke, M.M., Webb-
1045 Robertson, B.J., Chang, J., Luna, M.L., Long, C.E.*, et al.* (2013). Release of severe acute
1046 respiratory syndrome coronavirus nuclear import block enhances host transcription in human
1047 lung cells. Journal of virology *87*, 3885-3902.
1048
1049 Siu, K.L., Yeung, M.L., Kok, K.H., Yuen, K.S., Kew, C., Lui, P.Y., Chan, C.P., Tse, H., Woo, P.C.,
1050 Yuen, K.Y.*, et al.* (2014). Middle east respiratory syndrome coronavirus 4a protein is a double-
1051 stranded RNA-binding protein that suppresses PACT-induced activation of RIG-I and MDA5 in
1052 the innate antiviral response. Journal of virology *88*, 4866-4876.
1053
1054 Sola, I., Almazan, F., Zuniga, S., and Enjuanes, L. (2015). Continuous and Discontinuous RNA
1055 Synthesis in Coronaviruses. Annu Rev Virol *2*, 265-288.
1056
1057 Stark, G.R., and Darnell, J.E., Jr. (2012). The JAK-STAT pathway at twenty. Immunity *36*, 503-514.
1058
1059 Suthar, M.S., Shabman, R., Madric, K., Lambeth, C., and Heise, M.T. (2005). Identification of
1060 adult mouse neurovirulence determinants of the Sindbis virus strain AR86. Journal of virology
1061 *79*, 4219-4228.
1062
1063 Thi Nhu Thao, T., Labroussaa, F., Ebert, N., V'Kovski, P., Stalder, H., Portmann, J., Kelly, J.,
1064 Steiner, S., Holwerda, M., Kratzel, A.*, et al.* (2020). Rapid reconstruction of SARS-CoV-2 using a
1065 synthetic genomics platform. Nature *582*, 561-565.
1066
1067 Thornbrough, J.M., Jha, B.K., Yount, B., Goldstein, S.A., Li, Y., Elliott, R., Sims, A.C., Baric, R.S.,
1068 Silverman, R.H., and Weiss, S.R. (2016). Middle East Respiratory Syndrome Coronavirus NS4b
1069 Protein Inhibits Host RNase L Activation. mBio *7*.
1070
1071 Turner, R.B., Weingand, K.W., Yeh, C.H., and Leedy, D.W. (1998). Association between
1072 interleukin-8 concentration in nasal secretions and severity of symptoms of experimental
1073 rhinovirus colds. Clinical infectious diseases : an official publication of the Infectious Diseases
1074 Society of America *26*, 840-846.
1075
1076 Uhlén, M., Fagerberg, L., Hallström, B.M., Lindskog, C., Oksvold, P., Mardinoglu, A., Sivertsson,
1077 Å., Kampf, C., Sjöstedt, E., Asplund, A.*, et al.* (2015). Proteomics. Tissue-based map of the
1078 human proteome. Science *347*, 1260419.

1079
1080 Volk, A., Hackbart, M., Deng, X., Cruz-Pulido, Y., O'Brien, A., and Baker, S.C. (2020). Coronavirus
1081 Endoribonuclease and Deubiquitinating Interferon Antagonists Differentially Modulate the Host
1082 Response during Replication in Macrophages. Journal of virology *94*.
1083
1084 Wan, Y., Shang, J., Graham, R., Baric, R.S., and Li, F. (2020). Receptor recognition by novel
1085 coronavirus from Wuhan: An analysis based on decade-long structural studies of SARS. Journal
1086 of virology.
1087
1088 Weiss, S.R., and Navas-Martin, S. (2005). Coronavirus pathogenesis and the emerging pathogen
1089 severe acute respiratory syndrome coronavirus. Microbiology and molecular biology reviews :
1090 MMBR *69*, 635-664.
1091
1092 Whelan, J.N., Li, Y., Silverman, R.H., and Weiss, S.R. (2019). Zika Virus Production Is Resistant to
1093 RNase L Antiviral Activity. Journal of virology *93*.
1094
1095 Xia, H., Cao, Z., Xie, X., Zhang, X., Yun-Chung Chen, J., Wang, H., Menachery, V.D., Rajsbaum, R.,
1096 and Shi, P.-Y. (2020). Evasion of type-I interferon by SARS-CoV-2. Cell Reports *10*, 8234.
1097
1098 Xie, X., Muruato, A., Lokugamage, K.G., Narayanan, K., Zhang, X., Zou, J., Liu, J., Schindewolf, C.,
1099 Bopp, N.E., Aguilar, P.V*., et al.* (2020). An Infectious cDNA Clone of SARS-CoV-2. Cell host &
1100 microbe *27*, 841-848 e843.
1101
1102 Yamada, Y., and Liu, D.X. (2009). Proteolytic activation of the spike protein at a novel RRRR/S
1103 motif is implicated in furin-dependent entry, syncytium formation, and infectivity of
1104 coronavirus infectious bronchitis virus in cultured cells. Journal of virology *83*, 8744-8758.
1105
1106 Yang, W., Liu, Y., Slovik, K.J., Wu, J.C., Duncan, S.A., Rader, D.J., and Morrisey, E.E. (2015).
1107 Generation of iPSCs as a Pooled Culture Using Magnetic Activated Cell Sorting of Newly
1108 Reprogrammed Cells. PloS one *10*, e0134995.
1109
1110 Ye, Y., Hauns, K., Langland, J.O., Jacobs, B.L., and Hogue, B.G. (2007). Mouse hepatitis
1111 coronavirus A59 nucleocapsid protein is a type I interferon antagonist. Journal of virology *81*,
1112 2554-2563.
1113
1114 Zhao, L., Birdwell, L.D., Wu, A., Elliott, R., Rose, K.M., Phillips, J.M., Li, Y., Grinspan, J., Silverman,
1115 R.H., and Weiss, S.R. (2013). Cell-type-specific activation of the oligoadenylate synthetase-
1116 RNase L pathway by a murine coronavirus. Journal of virology *87*, 8408-8418.
1117
1118 Zhao, L., Jha, B.K., Wu, A., Elliott, R., Ziebuhr, J., Gorbalenya, A.E., Silverman, R.H., and Weiss,
1119 S.R. (2012). Antagonism of the interferon-induced OAS-RNase L pathway by murine coronavirus
1120 ns2 protein is required for virus replication and liver pathology. Cell host & microbe *11*, 607-
1121 616.
1122

1123 Zhao, L., Rose, K.M., Elliott, R., Van Rooijen, N., and Weiss, S.R. (2011). Cell-type-specific type I
1124 interferon antagonism influences organ tropism of murine coronavirus. Journal of virology *85*,
1125 10058-10068.
1126
1127 Zhou, A., Paranjape, J., Brown, T.L., Nie, H., Naik, S., Dong, B., Chang, A., Trapp, B., Fairchild, R.,
1128 Colmenares, C.*, et al.* (1997). Interferon action and apoptosis are defective in mice devoid of
1129 2',5'-oligoadenylate-dependent RNase L. The EMBO journal *16*, 6355-6363.
1130
1131 Zhou, P., Yang, X.L., Wang, X.G., Hu, B., Zhang, L., Zhang, W., Si, H.R., Zhu, Y., Li, B., Huang, C.L.,
1132 *et al.* (2020). A pneumonia outbreak associated with a new coronavirus of probable bat origin.
1133 Nature.
1134
1135 **Figure Legends**

1136 **Figure 1. Double-stranded RNA induced innate immune responses during SARS-CoV-2**
1137 **infection.** Coronavirus double-stranded RNA (dsRNA) is produced through replication and
1138 transcription and recognized by cytosolic OAS, MDA5, or PKR host receptors to activate innate
1139 immune pathways. MDA5 signals through MAVS, leading to type I and type III IFN production and
1140 release from the cell where it binds to cell surface receptors, which induces phosphorylation and
1141 heterodimerization of STAT1 and STAT2 that then prompt ISG transcription and cytokine
1142 responses. OASs produce 2'-5'-oligoadenylates (2-5A) that bind RNase L, leading to
1143 homodimerization and catalytic activation of RNase L, which cleaves host and viral ssRNA to
1144 trigger apoptosis and inflammation. PKR autophosphorylates before phosphorylating eIF2$\alpha$,
1145 which leads to translational arrest, cell death, and inflammatory responses. Graphic was created
1146 with Biorender.com
1147
1148

1149 **Figure 2. Infection of nasal epithelia-derived cells by SARS-CoV-2 and MERS-CoV.** Nasal
1150 cells were cultured in air-liquid trans-wells, and mock infected or infected with SARS-CoV-2
1151 (MOI=5), MERS-CoV (MOI=5) , or Sendai Virus (SeV) apically at MOI=10. (A) At indicated times,
1152 apically released virus was collected and quantified by plaque assay on Vero-E6 cells. Values are
1153 means ± SD (error bars). Statistical significance (not displayed) was determined by two-way

1154 ANOVA (*, $P < 0.05$). One experiment was performed using four separate donors. (B) At 48 hpi,
1155 nasal cells were fixed with 4% PFA and permeabilized. Expression of nucleocapsid (N) protein
1156 (red) of SARS-CoV-2 and MERS-CoV was detected with an anti-N antibody, and cilia (green) with
1157 an anti-type IV β-tubulin antibody by immunofluorescence assay (IFA). One representative image
1158 is shown from at least three independent experiments, with four donors for each virus infection
1159 shown. Scale bar = 100μm. (C) At 120 hpi, cells were lysed, and proteins were analyzed by
1160 immunoblotting with antibodies as indicated. One experiment using three separate donors was
1161 performed. (D) At 120 hpi, total RNA was harvested, and the mRNA expression level of *IFNB,*
1162 *IFNL1, OAS2, IFIT1, IFIH1, CXCL8* was quantified by RT-qPCR. Cycle threshold ($C_T$) values were
1163 normalized to 18S rRNA to generate $\Delta C_T$ values ($\Delta C_T = C_T$ gene of interest - $C_T$ 18S rRNA). Fold
1164 change over mock values were calculated by subtracting mock infected $\Delta C_T$ values from virus
1165 infected $\Delta C_T$ values, displayed as $2^{-\Delta(\Delta Ct)}$. Technical replicates were averaged, the means for each
1166 replicate displayed, ± SD (error bars). One experiment was performed using three separate donor
1167 samples. (E) Total RNA was harvested from two donors at 120 hpi and rRNA integrity determined
1168 by Bioanalyzer. The position of 28S and 18S rRNA and indicated. Data shown are from one
1169 representative experiment of two independent experiments. (See also Figures S1A&S2).
1170
1171 **Figure 3. Infection of iPSC-derived AT2 cells (iAT2) by SARS-CoV-2.** iAT2 cells were mock
1172 infected or infected with SARS-CoV-2 at MOI=5 or SINV at MOI=1. (A) At indicated times,
1173 supernatants were collected and infectious virus was quantified by plaque assay on Vero-E6 cells.
1174 Values are means ± SD (error bars). Data shown are one representative experiment from at least
1175 three independent experiments. (B) At 48 hpi, cells were fixed with 4% PFA and permeabilized.
1176 Expression of nucleocapsid (N) protein (green) of SARS-CoV-2 and the expression of SFTPC
1177 promoter control tdTomato fluorescent protein (AT2 marker in red) was examined by IFA.
1178 Channels are merged with DAPI nuclear staining. Images shown are representative from at least

1179 three independent experiments. Scale bar = 100μm. (C) At 48 hours post infection, cells were
1180 lysed and proteins were analyzed by immunoblotting with antibodies as indicated. Data shown are
1181 from one representative experiment of two independent experiments. (D) At 16 (SINV) or 48 (SARS-
1182 CoV-2) hpi, total RNA was harvested, and the mRNA expression level of *IFNB, IFNL1, OAS2,*
1183 *IFIT1, IFIH1, CXCL8* was quantified by RT-qPCR. $C_T$ values were normalized to 18S rRNA to
1184 generate $\Delta C_T$ values ($\Delta C_T$ = $C_T$ gene of interest - $C_T$ 18S rRNA). Fold change over mock values
1185 were calculated by subtracting mock infected $\Delta C_T$ values from virus infected $\Delta C_T$ values,
1186 displayed as $2^{-\Delta(\Delta Ct)}$. Technical replicates were averaged, the means for each replicate displayed,
1187 ± SD (error bars). Statistical significance was determined by Student *t* test (*, P < 0.05; **, P <
1188 0.01; ***, P < 0.001). Data shown are from one representative experiment of two independent
1189 experiments. (E) Total RNA was harvested at 16 (SINV) or 48 (SARS-CoV-2) hpi and rRNA integrity
1190 determined by Bioanalyzer. The position of 28S and 18S rRNA and indicated. Data shown are from
1191 one representative experiment of two independent experiments. (See also Figures S1B&S2).
1192
1193 **Figure 4. Infection of iPSC-derived cardiomyocytes (iCM) by SARS-CoV-2.** iCM were mock
1194 infected or infected at MOI=1 with SARS-CoV-2 or SINV. (A) At indicated times, supernatants
1195 were collected and virus quantified by plaque assay on Vero-E6 cells. Values are means ± SD
1196 (error bars). Data shown are one representative experiment from at least three independent
1197 experiments. (B) At 48 hpi, iCM were fixed with 4% PFA and permeabilized, the expression of
1198 SARS-CoV-2 N (green) of and of cTnT protein (cardiomyocyte marker, red) was examined by
1199 IFA. Channels are merged with DAPI nuclear staining. Images shown are representative from
1200 three independent experiments. Scale bar = 50μm. (C) At 16 (SINV) or 48 (SARS-CoV-2) hpi,
1201 cells were lysed and proteins were analyzed by immunoblotting with antibodies as indicated.
1202 Immunoblots were performed at least two times and one representative blot is shown. (D) At 16
1203 (SINV) or 48 (SARS-CoV-2) hpi, total RNA was harvested, the mRNA expression level of *IFNB,*

1204 *IFNL1, OAS2, IFIT1, IFIH1, CXCL8* was quantified by RT-qPCR. $C_T$ values were normalized to
1205 18S rRNA to generate $\Delta C_T$ values ($\Delta C_T$ = $C_T$ gene of interest - $C_T$ 18S rRNA). Fold change over
1206 mock values were calculated by subtracting mock infected $\Delta C_T$ values from virus infected $\Delta C_T$
1207 values, displayed as $2^{-\Delta(\Delta Ct)}$. Technical replicates were averaged, the means for each replicate
1208 displayed, ± SD (error bars). Statistical significance was determined by Student *t* test (*, P < 0.05;
1209 ****, P < 0.0001; ns = not significant). Data shown are from one representative experiment of two
1210 independent experiments. (E) Total RNA was harvested at 16 (SINV) or 48 (SARS-CoV-2) hpi, and
1211 rRNA integrity determined by Bioanalyzer. The position of 28S and 18S rRNA and indicated. Data
1212 shown are from one representative experiment of two independent experiments. (See also Figures
1213 S1C&S2).
1214
1215 **Figure 5. Replication of SARS-CoV-2 in A549$^{ACE2}$ and Calu-3 cell lines.** (A) Vero-E6 or
1216 A549$^{ACE2}$ cells were infected with SARS-CoV-2 at MOI=1. At the indicated times, supernatant was
1217 collected and virus quantified by plaque assay on Vero-E6 cells. Values are means ± SD (error
1218 bars). (B) Calu-3 cells were infected with SARS-CoV-2, MERS-CoV or MERS-CoV-ΔNS4ab at
1219 MOI=1. Supernatant was collected at the indicated times and virus quantified by plaque assay on
1220 Vero-E6 cells (SARS-CoV-2) or VeroCCL81 cells (MERS-CoV and MERS-CoV-Δ4ab). Values
1221 represent means ± SEM (error bars). Statistical significance was determined by Student *t* test (**,
1222 P < 0.01). Data shown are one representative experiment of three independent experiments. (C)
1223 Vero-E6, A549$^{ACE2}$, and Calu-3 cells were grown on untreated (Vero-E6 and A549$^{ACE2}$) or
1224 collagen-coated (Calu-3) glass coverslips before infection with SARS-CoV-2 at MOI = 1. At
1225 indicated hpi, cells were fixed with 4% PFA and permeabilized for N (green) and dsRNA (red)
1226 expression detection by IFA using anti-N and J2 antibodies, respectively. Channels are merged
1227 with DAPI nuclear staining. Images shown are representative from two independent experiments.
1228 Scale bar = 25μm. (See also Figure S3&S4A).

1229

1230 **Figure 6. SARS-CoV-2 IFN responses in the lung epithelia-derived A549$^{ACE2}$ cell line.**
1231 A549$^{ACE2}$ cells were mock infected or infected with SINV (MOI=1) or SARS-CoV-2 (MOI=5). (A)
1232 Total RNA was harvested at 24 and 48 hpi. Expression of *IFNB, IFNL1, OAS2, IFIT1, IFIH1,* and
1233 *CXCL8* mRNA was quantified by RT-qPCR. $C_T$ values were normalized to 18S rRNA to generate
1234 $\Delta C_T$ values ($\Delta C_T$ = $C_T$ gene of interest - $C_T$ 18S rRNA). Fold change over mock values were
1235 calculated by subtracting mock infected $\Delta C_T$ values from virus infected $\Delta C_T$ values, displayed as
1236 $2^{-\Delta(\Delta Ct)}$. Technical replicates were averaged, the means for each replicate displayed, ± SD (error
1237 bars). (B) Viral genome copies per ug of total RNA were calculated at 24 and 48hpi by RT-qPCR
1238 standard curve generated using a digested plasmid encoding SARS-CoV-2 nsp12. Values are
1239 means ± SD (error bars). Statistical significance was determined by one-way ANOVA (*, P < 0.05;
1240 **, P < 0.01; ***, P < 0.001; ****, P < 0.0001; ns = not significant). (C) At 24 hpi, A549$^{ACE2}$ cells
1241 were lysed and proteins harvested. Protein expression was analyzed by immunoblot using the
1242 indicated antibodies. All data are one representative experiment of three independent
1243 experiments. (See also Figures S2 and S4B&C).

1244

1245 **Figure 7. SARS-CoV-2 and MERS-CoV IFN responses in the lung-derived Calu-3 cells.** Calu-
1246 3 cells were mock treated or infected with SARS-CoV-2, MERS-CoV or MERS-CoV-ΔNS4ab at
1247 MOI=5. (A) At 24 or 48 hpi, total RNA was harvested. Expression of *IFNB, IFNL1, OAS2, IFIT1,*
1248 *IFIH1,* and *CXCL8* mRNA was quantified by RT-qPCR. $C_T$ values were normalized to 18S rRNA
1249 to generate $\Delta C_T$ values ($\Delta C_T$ = $C_T$ gene of interest - $C_T$ 18S rRNA). Fold change over mock values
1250 were calculated by subtracting mock infected $\Delta C_T$ values from virus infected $\Delta C_T$ values,
1251 displayed as $2^{-\Delta(\Delta Ct)}$. Technical replicates were averaged, the means for each replicate displayed,
1252 ± SD (error bars). Statistical significance was determined by two-way ANOVA (*, P < 0.05; **, P
1253 < 0.01; ***, P < 0.001; ****, P < 0.0001; ns = not significant). (B) Viral genome copies per ug of

1254 total RNA were calculated by RT-qPCR standard curve generated using a digested plasmid
1255 encoding SARS-CoV-2 nsp12 or plasmid encoding a region of MERS-CoV orf1ab. Values are
1256 means ± SD (error bars). Statistical significance was determined by two-way ANOVA (*, $P < 0.05$;
1257 **, $P < 0.01$; ns = not significant). (C) At 24 hpi, Calu-3 cells were lysed and proteins harvested.
1258 Proteins were analyzed by immunoblotting using the indicated antibodies. All data are one
1259 representative experiment of three independent experiments. (See Figure S2).
1260
1261 **Figure 8. SARS-CoV-2 infection leads to activation of RNase L and PKR in A549$^{ACE2}$ and**
1262 **Calu-3 cells.** A549$^{ACE2}$ and Calu-3 cells were mock infected or infected with SARS-CoV-2, MERS-
1263 CoV, or MERS-CoV-ΔNS4ab at MOI=5. Total RNA was harvested from A549$^{ACE2}$ cells (A) or
1264 Calu-3 cells (B) at 24 and 48 hpi. 28S and 18S rRNA integrity was assessed by Bioanalyzer. 28S
1265 and 18s rRNA bands are indicated. At 24 hpi, A549$^{ACE2}$ cells (C) or Calu-3 cells (D) were lysed
1266 and proteins harvested for analysis by immunoblotting using the indicated antibodies. All data are
1267 one representative experiment of three independent experiments. (See also Figure S4D&E).
1268
1269 **Figure 9. Replication of SARS-CoV-2 is restricted by RNase L independent of PKR or**
1270 **MAVS.** Indicated genes were knocked out (KO) from one clone of A549$^{ACE2}$ cells using CRISPR-
1271 Cas9 engineering. (A) KO cell lines were grown in culture with or without 1000U IFN-α treatment
1272 for 24 hours. Cells were lysed and proteins harvested for analysis by immunoblotting using
1273 indicated antibodies. (B) Indicated cell lines were infected with SARS-CoV-2 at MOI=1. At the
1274 indicated time points, supernatant was collected and virus quantified by plaque assay on Vero-
1275 E6 cells. Values represent mean ± SD (error bars). Statistical significance was determined by
1276 two-way ANOVA (****, $P < 0.0001$; ns = not significant). Data are one representative experiment
1277 from at least three independent experiments. (C) Indicated cell lines were mock treated or infected
1278 with SARS-CoV-2 at MOI=1. At 48 hpi, cells were fixed with 4% PFA and stained with 1% crystal
1279 violet as a marker for live cells. The image is one representative experiment from two independent

1280 experiments. (D) The indicated cell lines were mock infected or infected with SARS-CoV-2 or
1281 SINV at MOI=1. RNA was harvested 24 hpi (SINV) or 24 and 48 hpi (SARS-CoV-2). Integrity of
1282 rRNA was assessed by Bioanalyzer. 28S and 18S rRNA bands are indicated. Data is one
1283 representative experiment of two independent experiments.
1284
1285 **Figure S1. Genome replication in nasal cells, iAT2, and iCM.** Nasal (A) and iAT2 cells (B)
1286 were infected at MOI=5 with SARS-CoV-2, and (C) iCM at MOI=1 with SARS-CoV-2 or SINV.
1287 Total RNA was harvested at 48 hpi(SARS-COV-2) or 16 hpi(SINV) for iAT2 and iCM cells and
1288 120 hpi for nasal cells. Viral genome copies per ug of harvested RNA were calculated by RT-
1289 qPCR standard curve generated using a digested plasmid encoding SARS-CoV-2 nsp12. Values
1290 are means ± SD (error bars). For SINV (C), cycle threshold ($C_T$) values of SINV nsP4 polymerase
1291 sequences were normalized to 18S rRNA to generate $\Delta C_T$ values ($\Delta C_T$ = $C_T$ gene of interest - $C_T$
1292 18S rRNA). Technical triplicates were averaged and displayed using the equation $2^{-(\Delta CT)}$. Data are
1293 from one representative experiment of two independent experiments.
1294
1295 **Figure S2. Host basal mRNA expression of uninfected cells.** Total RNA was harvested from
1296 mock treatment from all indicated cell types after 24 hours incubation. mRNA expression levels
1297 of *IFNB, IFNL1, OAS2, IFIT1, IFHI1,* and *CXCL8* were quantified by RT-qPCR. $C_T$ values were
1298 normalized to 18S rRNA to generate $\Delta C_T$ values ($\Delta C_T$ = $C_T$ gene of interest - $C_T$ 18S rRNA). (A)
1299 Basal level of gene expression is displayed for nasal cells, iAT2 and iCM, Calu-3 cells and two
1300 clones of $A549^{ACE2}$ cells, displayed as $2^{-\Delta Ct}$. (B) Fold expression over $A549^{ACE2}$ C44 values were
1301 calculated by subtracting $\Delta C_T$ values from the indicated cell line from $A549^{ACE2}$ C44 $\Delta C_T$ values,
1302 displayed as $2^{-\Delta(\Delta CT)}$. Biological replicates were averaged and values are means ± SD (error bars).
1303 Data were generated from at least two independent experiments.
1304

1305 **Figure S3. ACE2 protein expression in A549$^{ACE2}$ and Calu-3 cell lines.** Parental A549 cells,
1306 two A549$^{ACE2}$ clones, and Calu-3 cells were grown in culture before lysis and protein harvest.
1307 Protein expression was analyzed by immunoblotting using the indicated antibodies.
1308
1309 **Figure S4. SARS-CoV-2 replication and host responses in a second lung epithelia-derived**
1310 **A549$^{ACE2}$ cell line clone (C34).** (A) Vero-E6 or A549$^{ACE2}$ cells were infected with SARS-CoV-2 at
1311 MOI=1 and supernatant harvested at indicated times post infection. Infectious virus was quantified
1312 by plaque assay on Vero-E6 cells. Values are means ± SD (error bars). (B) A549$^{ACE2}$ cells (C34)
1313 were mock infected or infected with SARS-CoV-2 or SINV at MOI=5 and total RNA total RNA
1314 harvested at 24 (SINV) or 24 and 48 (SARS-CoV-2) hpi. Expression of *IFNB, IFNL1, OAS2, IFIT1,*
1315 *IFIH1,* and *CXCL8* mRNA was quantified by RT-qPCR. $C_T$ values were normalized to 18S rRNA
1316 to generate $\Delta C_T$ values ($\Delta C_T = C_T$ gene of interest - $C_T$ 18S rRNA). Fold change over mock values
1317 were calculated by subtracting mock infected $\Delta C_T$ values from virus infected $\Delta C_T$ values,
1318 displayed as $2^{-\Delta(\Delta Ct)}$. Statistical significance for each gene was determined by one-way ANOVA
1319 (***, $P < 0.001$; ****, $P < 0.0001$; ns = not significant). Technical replicates were averaged, the
1320 means for each replicate displayed, ± SD (error bars). (C&D) A549$^{ACE2}$ cells were infected at
1321 MOI=5, lysed at 24 hpi, and proteins harvested for analysis by immunoblotting using the indicated
1322 antibodies. (E) A549$^{ACE2}$ cells were infected at MOI=1 (SINV) or MOI=5 (SARS-CoV-2) and total
1323 RNA harvested at 24 (SINV) or 24 and 48 (SARS-CoV-2) hpi. Integrity of rRNA was assessed by
1324 Bioanalyzer. 28S and 18s rRNA bands are indicated. All data are representative of two or three
1325 independent experiments.
1326

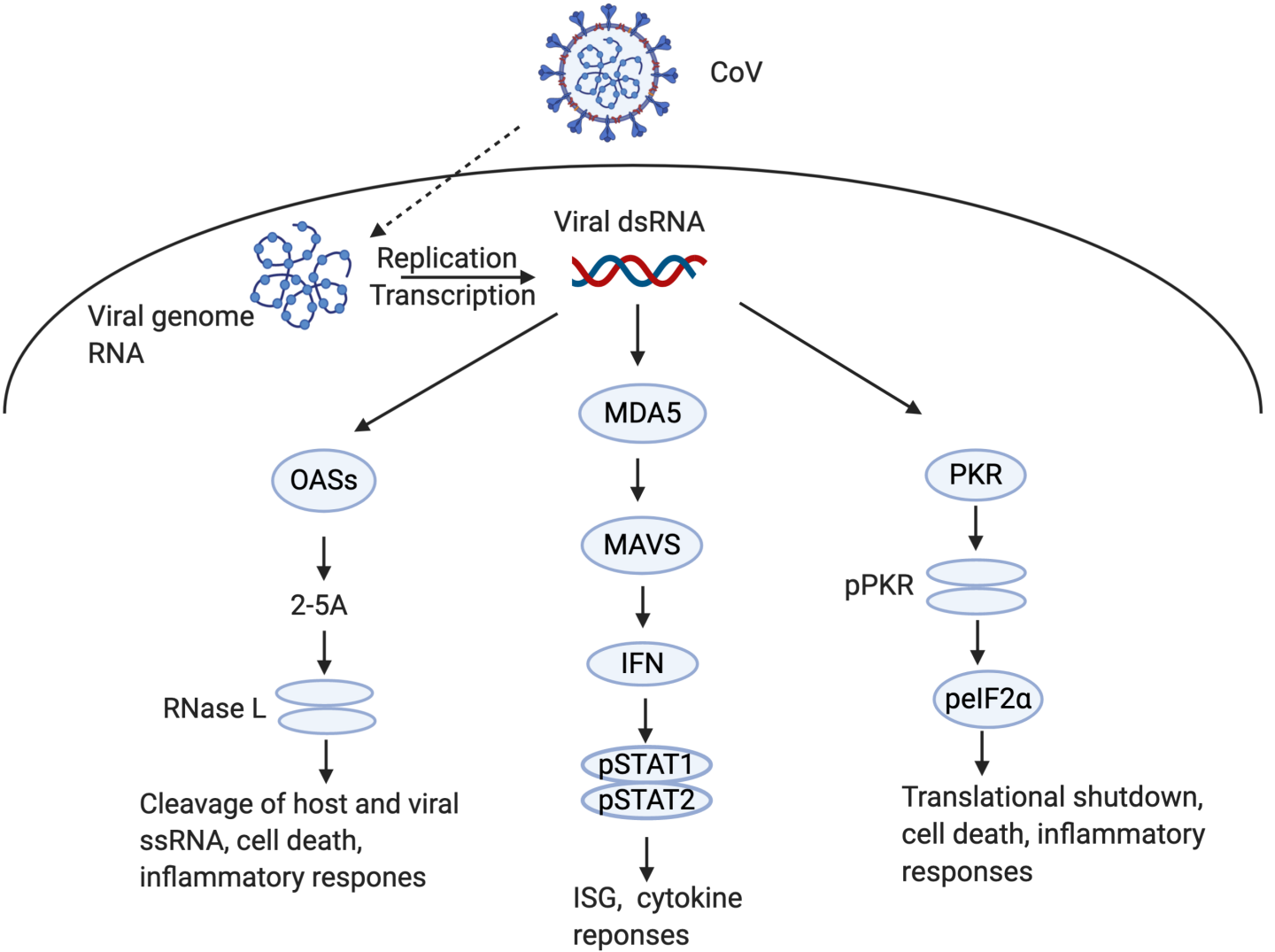
CoV
Viral dsRNA
Replication
Transcription
Viral genome
RNA
OASs
2-5A
RNase L
Cleavage of host and viral
ssRNA, cell death,
inflammatory respones
MDA5
MAVS
IFN
pSTAT1
pSTAT2
ISG, cytokine
reponses
PKR
pPKR
peIF2α
Translational shutdown,
cell death, inflammatory
responses

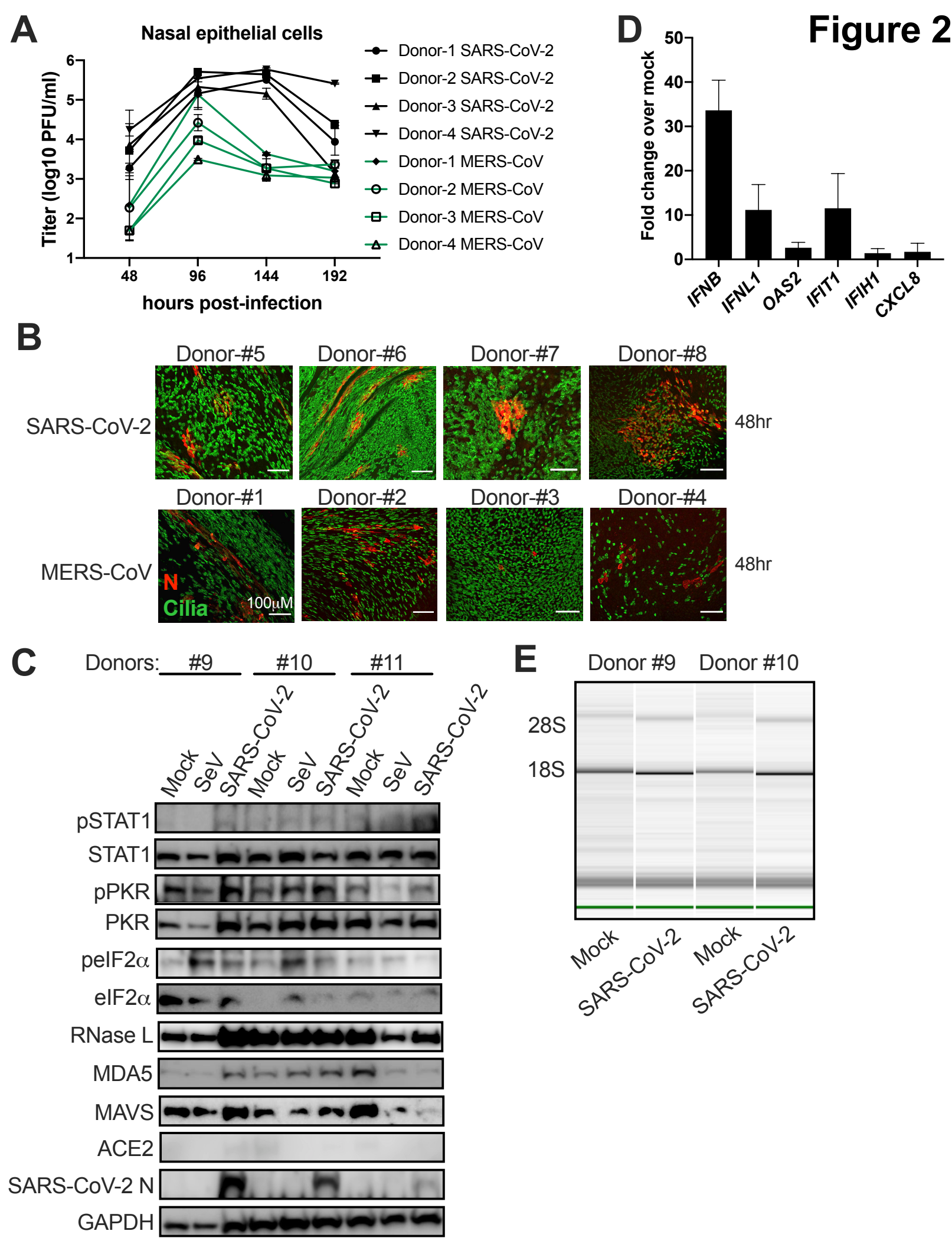
Figure 2
A
Nasal epithelial cells
Titer (log10 PFU/ml)
hours post-infection
48
96
144
192
Donor-1 SARS-CoV-2
Donor-2 SARS-CoV-2
Donor-3 SARS-CoV-2
Donor-4 SARS-CoV-2
Donor-1 MERS-CoV
Donor-2 MERS-CoV
Donor-3 MERS-CoV
Donor-4 MERS-CoV
D
Fold change over mock
IFNB
IFNL1
OAS2
IFIT1
IFIH1
CXCL8
B
Donor-#5
Donor-#6
Donor-#7
Donor-#8
SARS-CoV-2
48hr
Donor-#1
Donor-#2
Donor-#3
Donor-#4
MERS-CoV
N
Cilia
100μM
48hr
C
Donors: #9 #10 #11
Mock
SeV
SARS-CoV-2
pSTAT1
STAT1
pPKR
PKR
peIF2α
eIF2α
RNase L
MDA5
MAVS
ACE2
SARS-CoV-2 N
GAPDH
E
Donor #9
Donor #10
28S
18S
Mock
SARS-CoV-2

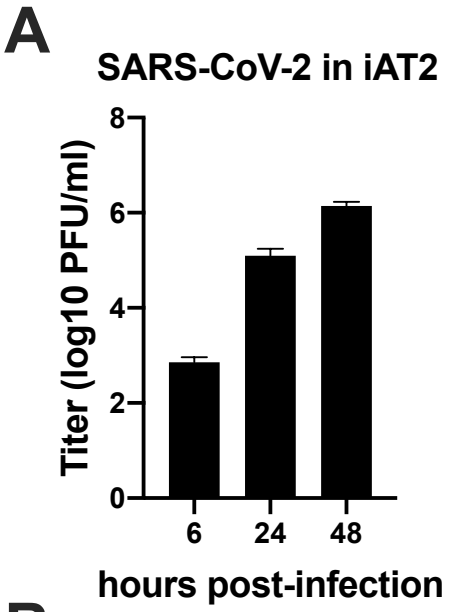
A
SARS-CoV-2 in iAT2
Titer (log10 PFU/ml)
0
2
4
6
8
6
24
48
hours post-infection

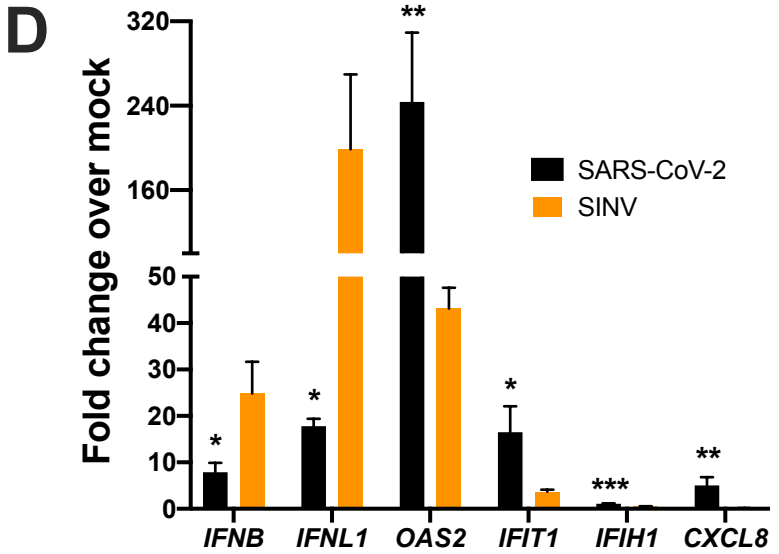
D
Fold change over mock
320
240
160
50
40
30
20
10
0
SARS-CoV-2
SINV
*
*
**
*
***
**
IFNB
IFNL1
OAS2
IFIT1
IFIH1
CXCL8

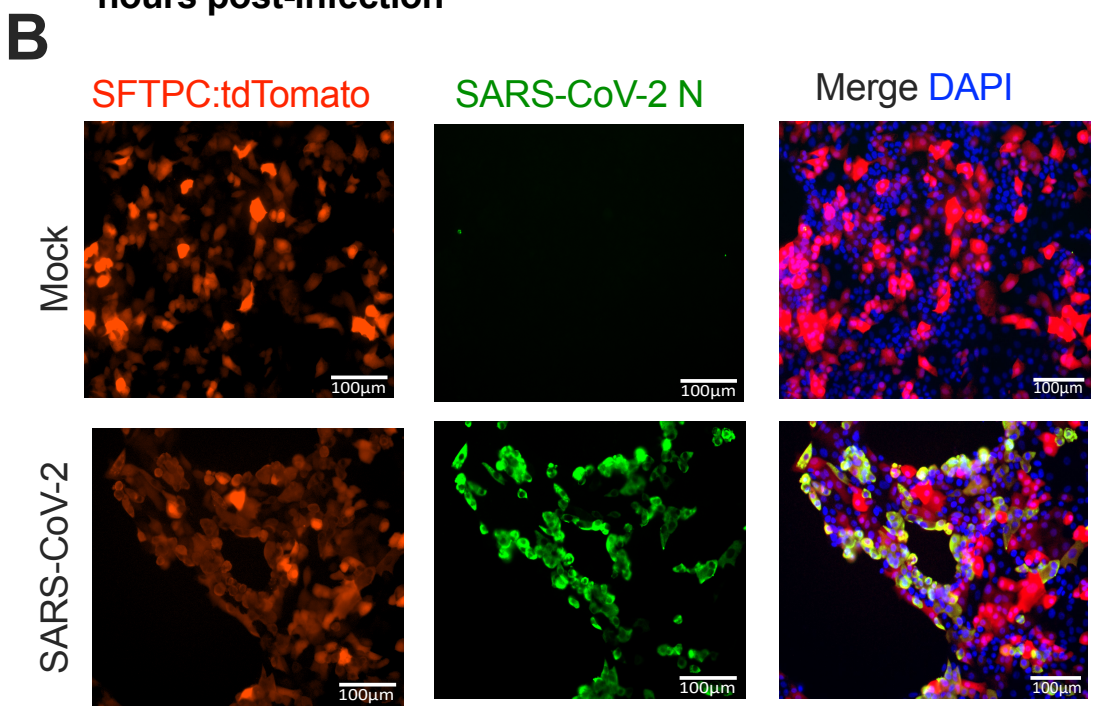
B
SFTPC:tdTomato
SARS-CoV-2 N
Merge DAPI
Mock
SARS-CoV-2
100µm

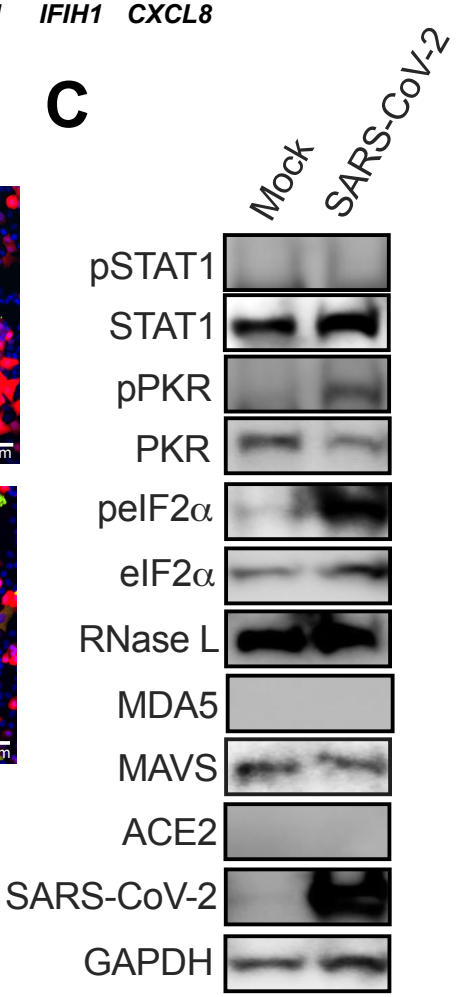
C
Mock
SARS-CoV-2
pSTAT1
STAT1
pPKR
PKR
peIF2α
eIF2α
RNase L
MDA5
MAVS
ACE2
SARS-CoV-2
GAPDH

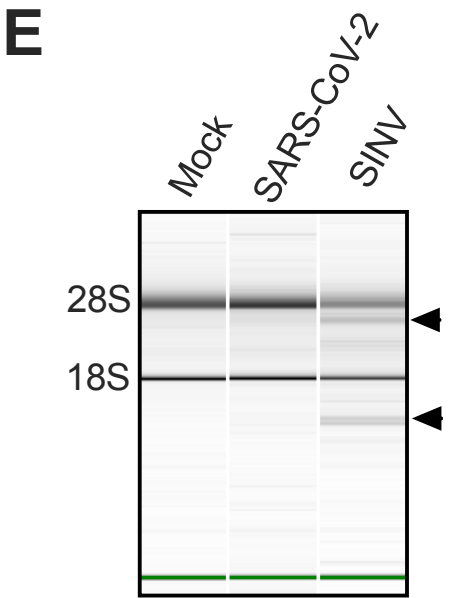
E
Mock
SARS-CoV-2
SINV
28S
18S

**Figure 3**

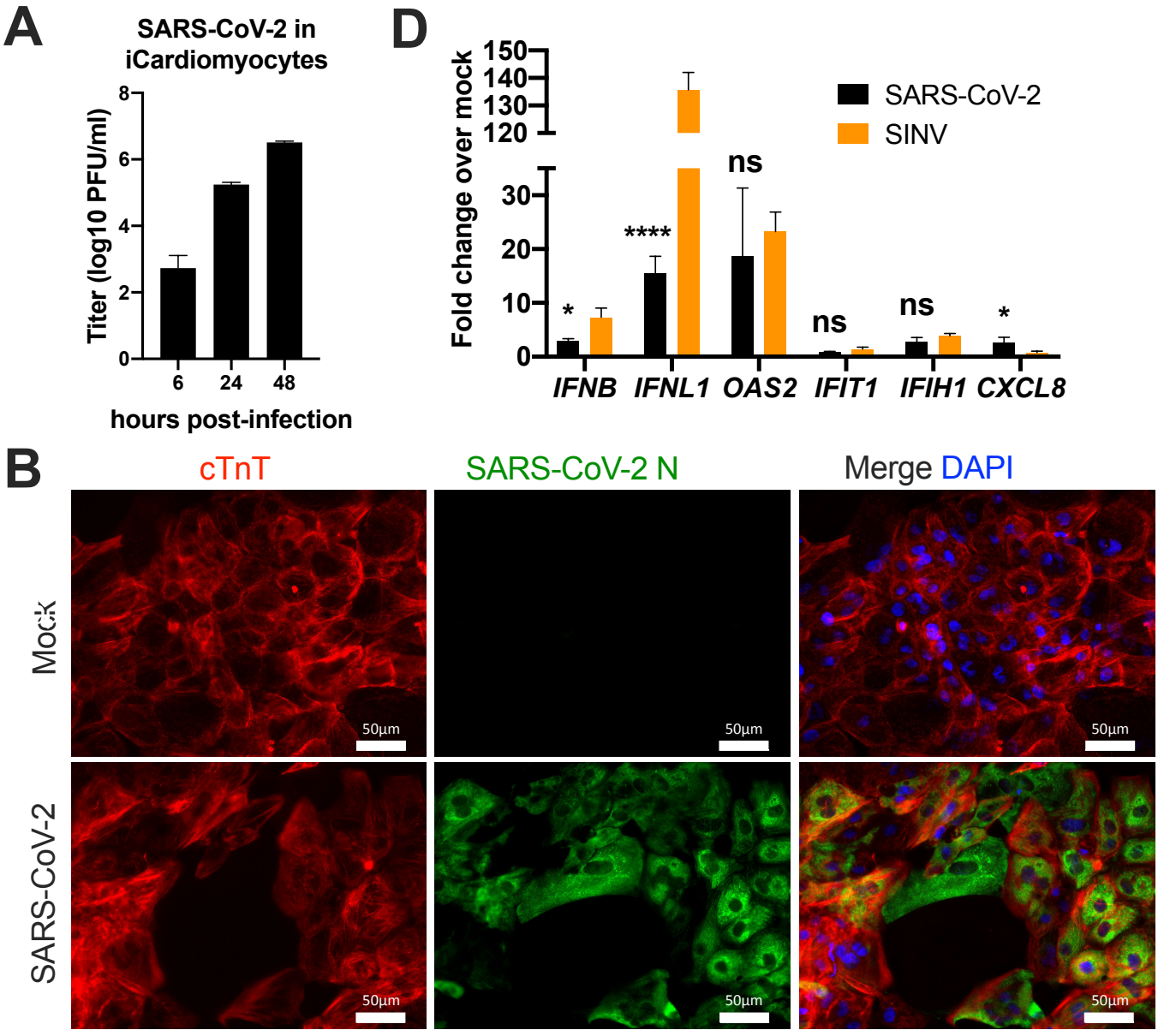
A
SARS-CoV-2 in iCardiomyocytes
Titer (log10 PFU/ml)
0
2
4
6
8
6
24
48
hours post-infection
D
Fold change over mock
150
140
130
120
30
20
10
0
SARS-CoV-2
SINV
*
****
ns
ns
ns
*
IFNB
IFNL1
OAS2
IFIT1
IFIH1
CXCL8
B
cTnT
SARS-CoV-2 N
Merge DAPI
Mock
SARS-CoV-2
50µm

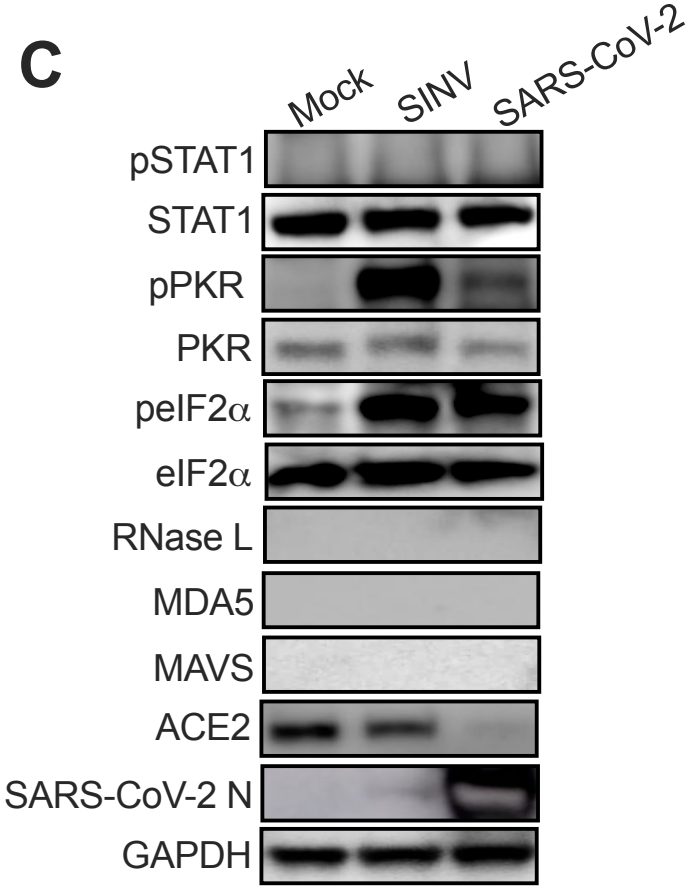
C
Mock
SINV
SARS-CoV-2
pSTAT1
STAT1
pPKR
PKR
peIF2α
eIF2α
RNase L
MDA5
MAVS
ACE2
SARS-CoV-2 N
GAPDH

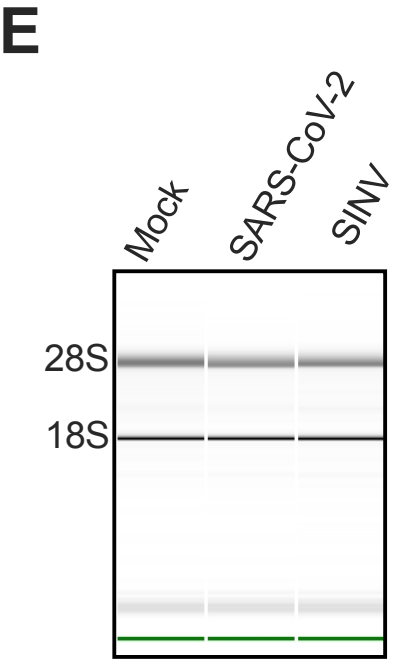
E
Mock
SARS-CoV-2
SINV
28S
18S

**Figure 4**

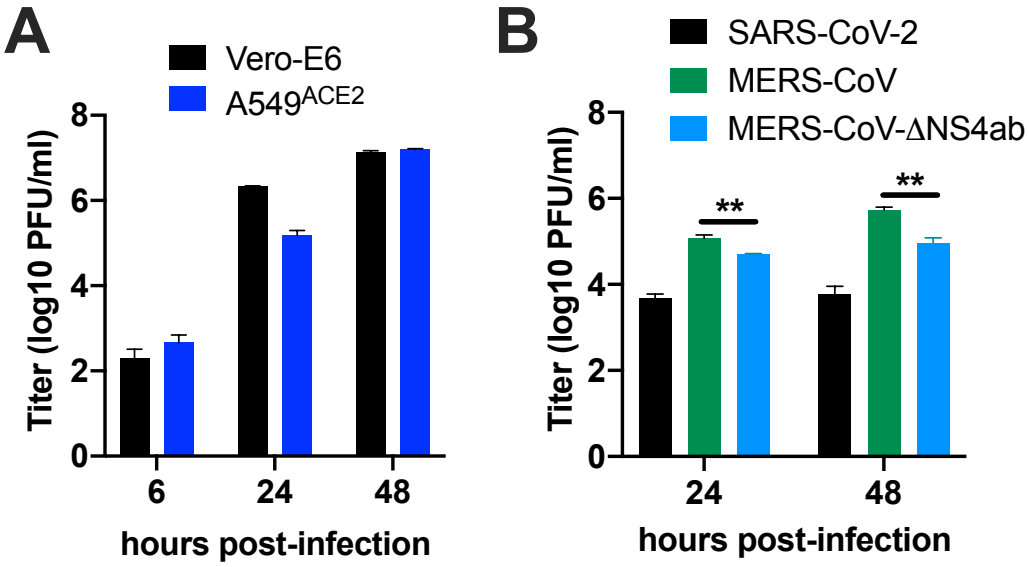
A
Vero-E6
A549ACE2
Titer (log10 PFU/ml)
0
2
4
6
8
6
24
48
hours post-infection
B
SARS-CoV-2
MERS-CoV
MERS-CoV-ΔNS4ab
Titer (log10 PFU/ml)
0
2
4
6
8
**
**
24
48
hours post-infection

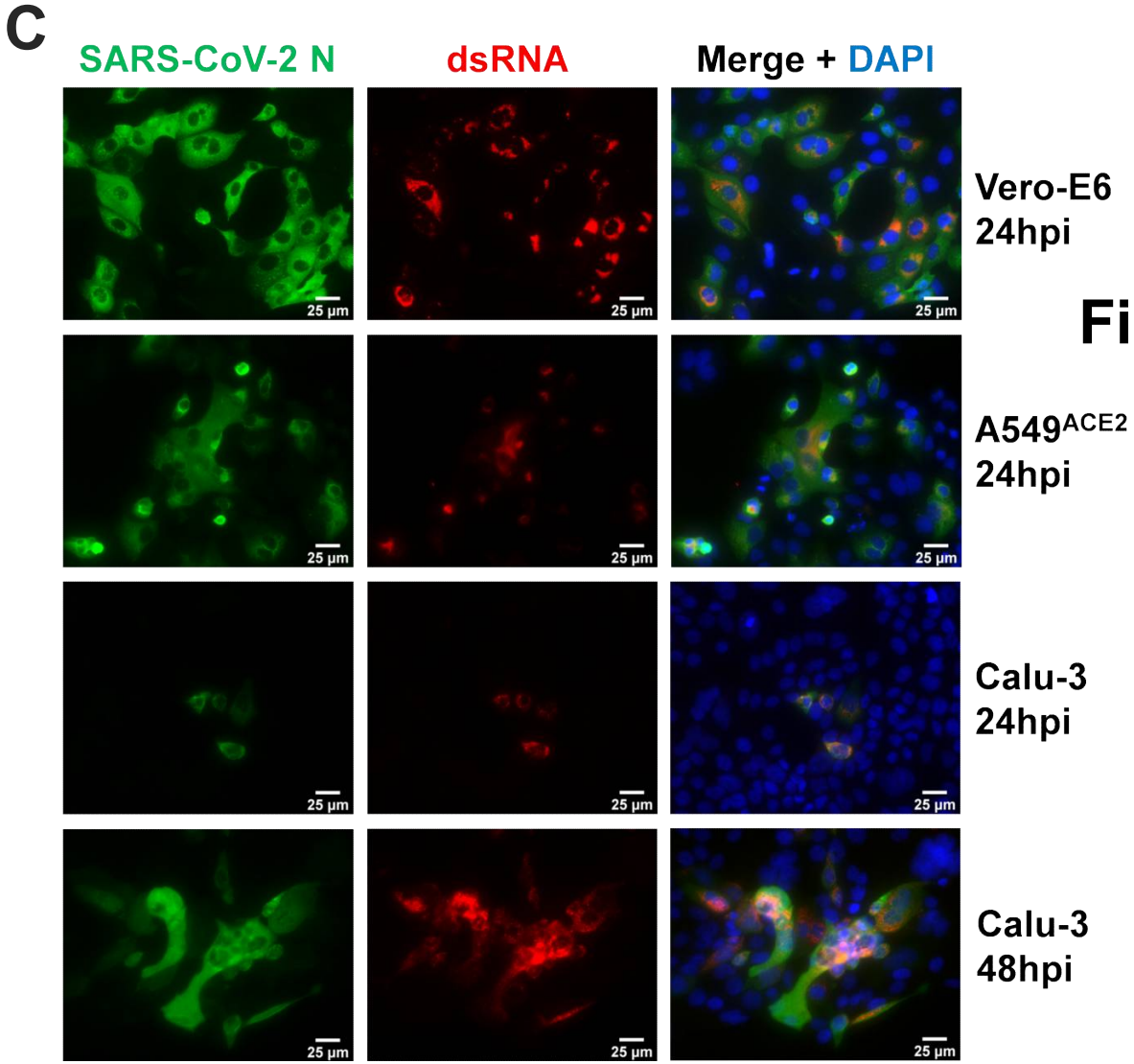
C
SARS-CoV-2 N
dsRNA
Merge + DAPI
Vero-E6
24hpi
A549ACE2
24hpi
Calu-3
24hpi
Calu-3
48hpi
25 µm

Figure 5

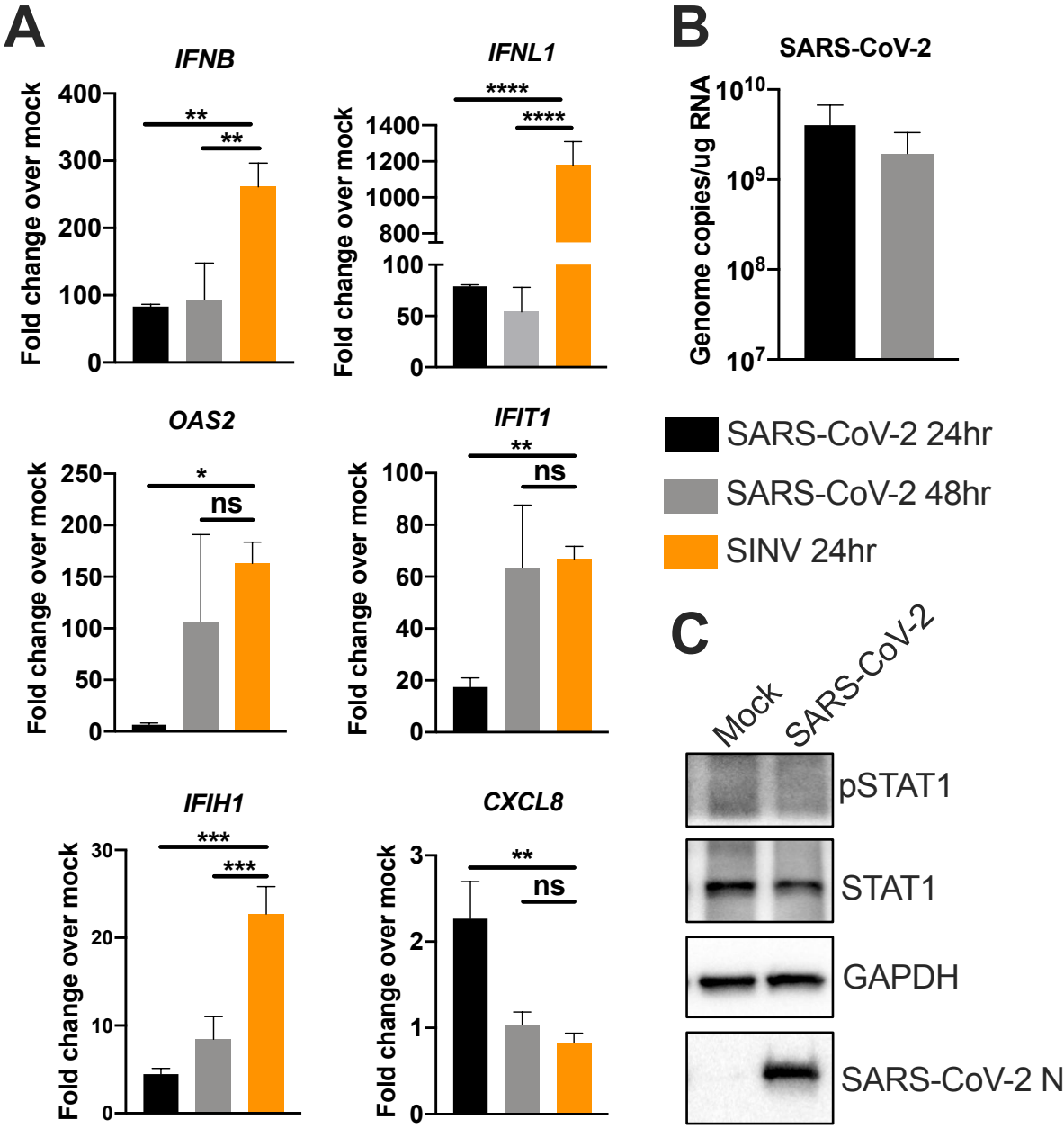
A
IFNB
Fold change over mock
400
300
200
100
0
**
**
IFNL1
Fold change over mock
1400
1200
1000
800
100
50
0
****
****
OAS2
Fold change over mock
250
200
150
100
50
0
*
ns
IFIT1
Fold change over mock
100
80
60
40
20
0
**
ns
IFIH1
Fold change over mock
30
20
10
0
***
***
CXCL8
Fold change over mock
3
2
1
0
**
ns
B
SARS-CoV-2
Genome copies/ug RNA
$10^{10}$
$10^{9}$
$10^{8}$
$10^{7}$
SARS-CoV-2 24hr
SARS-CoV-2 48hr
SINV 24hr
C
Mock
SARS-CoV-2
pSTAT1
STAT1
GAPDH
SARS-CoV-2 N

# Figure 6

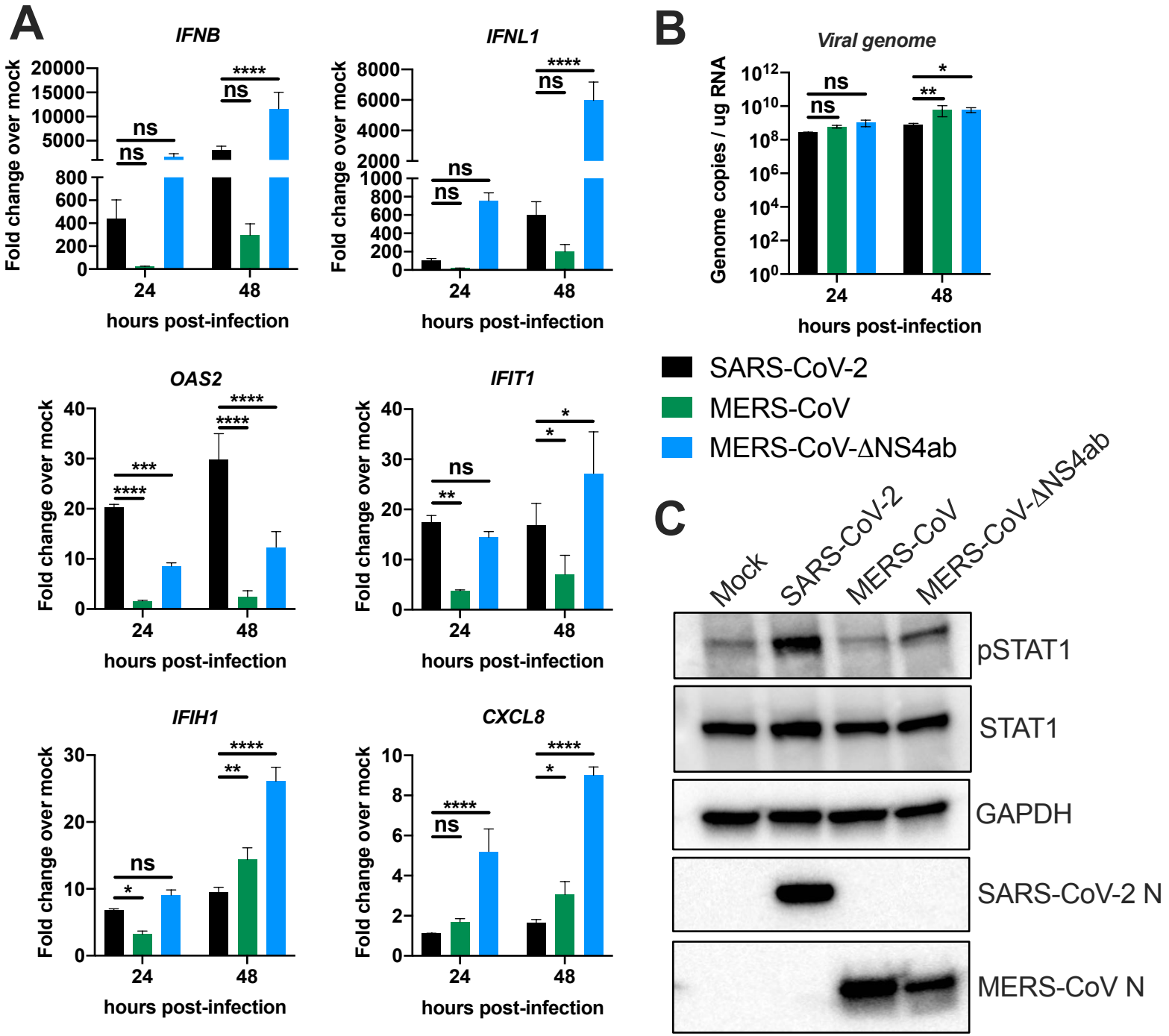
A
IFNB
IFNL1
OAS2
IFIT1
IFIH1
CXCL8
Fold change over mock
hours post-infection
24
48
ns
B
Viral genome
Genome copies / ug RNA
SARS-CoV-2
MERS-CoV
MERS-CoV-ΔNS4ab
C
Mock
SARS-CoV-2
MERS-CoV
MERS-CoV-ΔNS4ab
pSTAT1
STAT1
GAPDH
SARS-CoV-2 N
MERS-CoV N

Figure 7

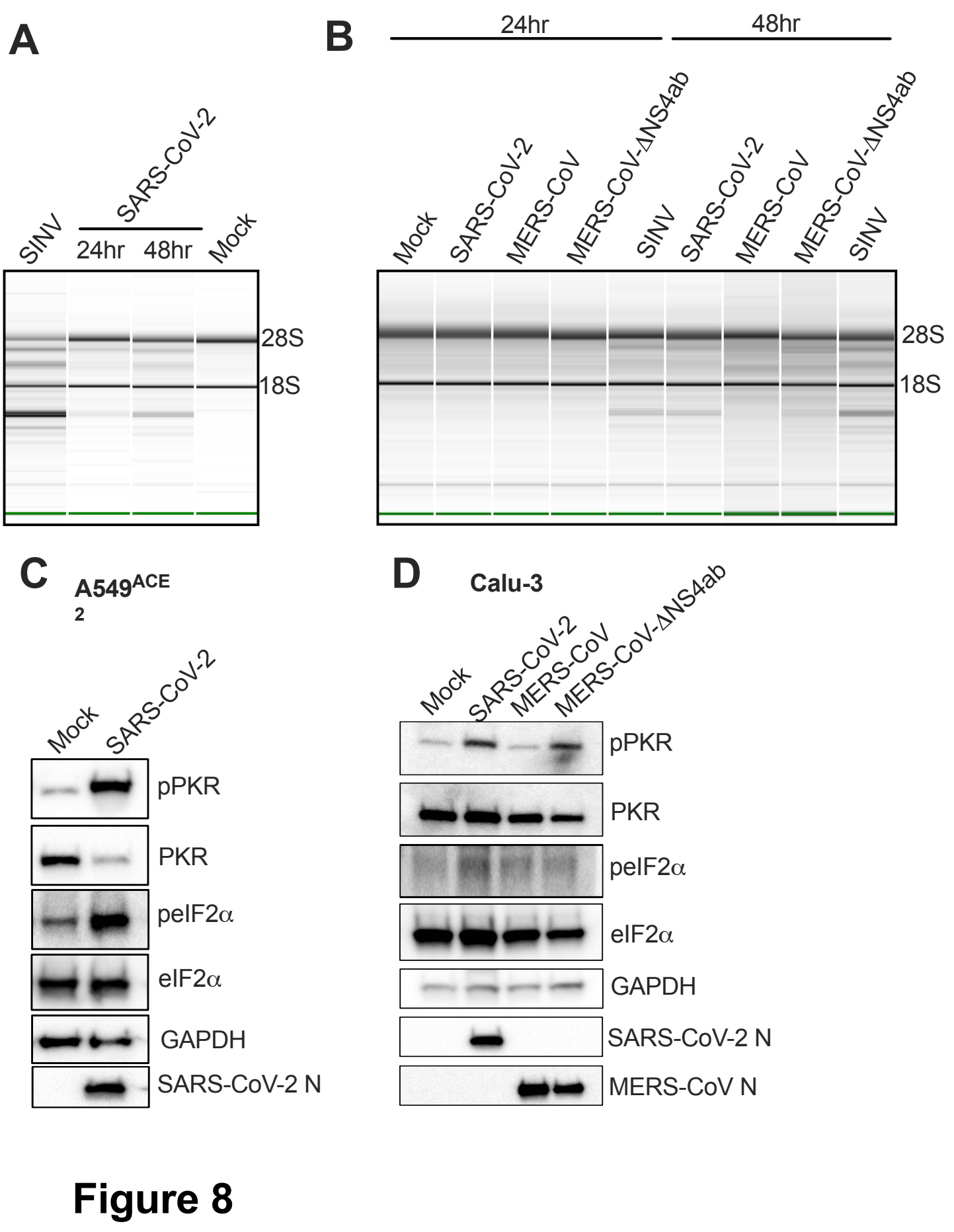
A
SINV
SARS-CoV-2
24hr
48hr
Mock
28S
18S
B
24hr
48hr
Mock
SARS-CoV-2
MERS-CoV
MERS-CoV-ΔNS4ab
SINV
SARS-CoV-2
MERS-CoV
MERS-CoV-ΔNS4ab
SINV
28S
18S
C
A549ACE2
Mock
SARS-CoV-2
pPKR
PKR
peIF2α
eIF2α
GAPDH
SARS-CoV-2 N
D
Calu-3
Mock
SARS-CoV-2
MERS-CoV
MERS-CoV-ΔNS4ab
pPKR
PKR
peIF2α
eIF2α
GAPDH
SARS-CoV-2 N
MERS-CoV N

**Figure 8**

# Figure 9

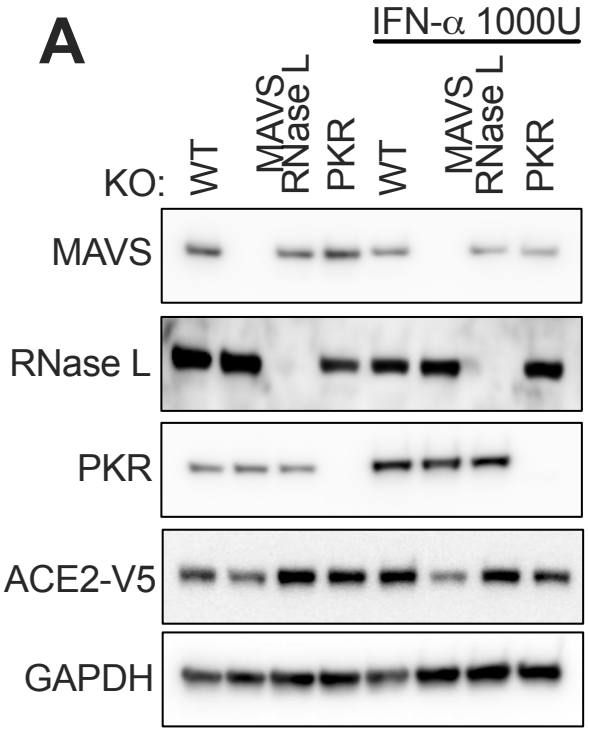


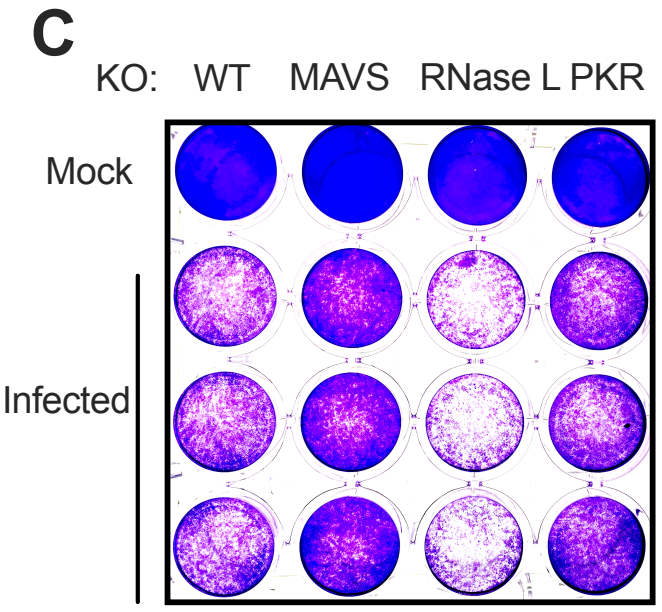


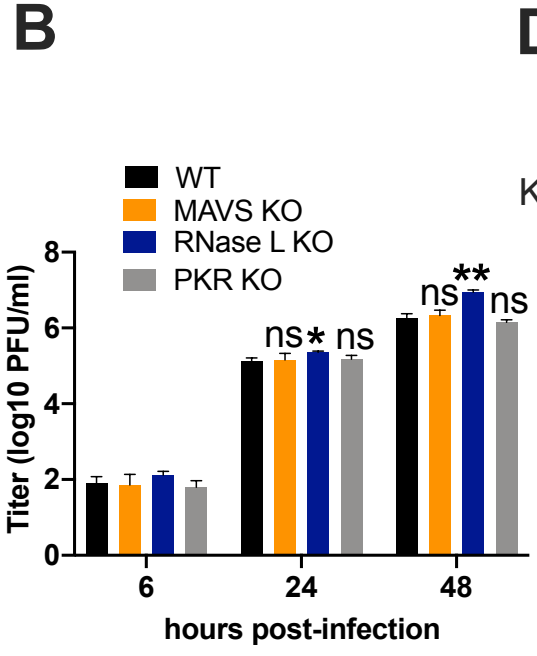


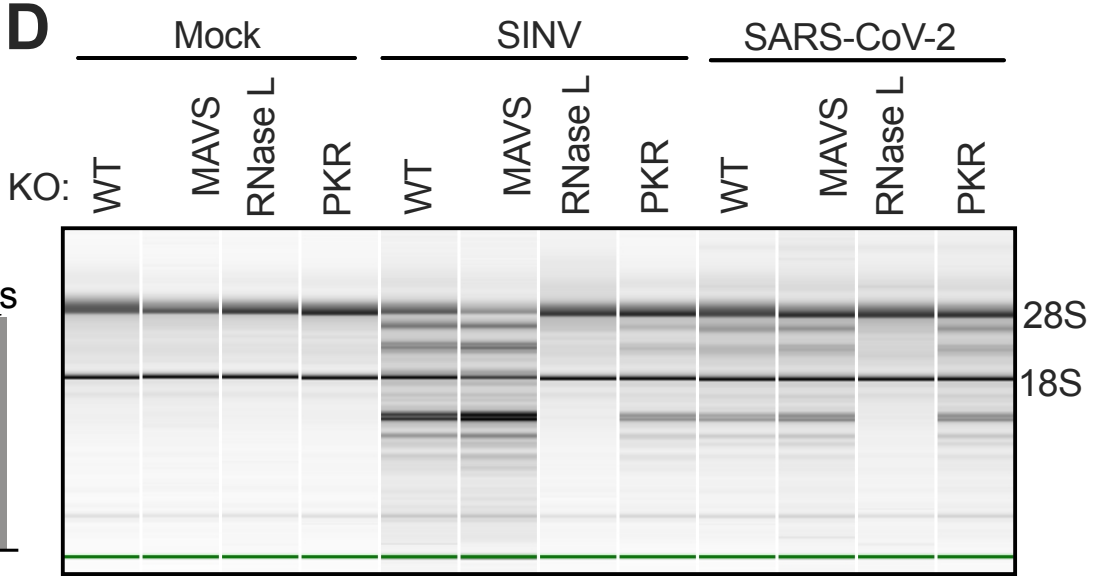


Figure 9

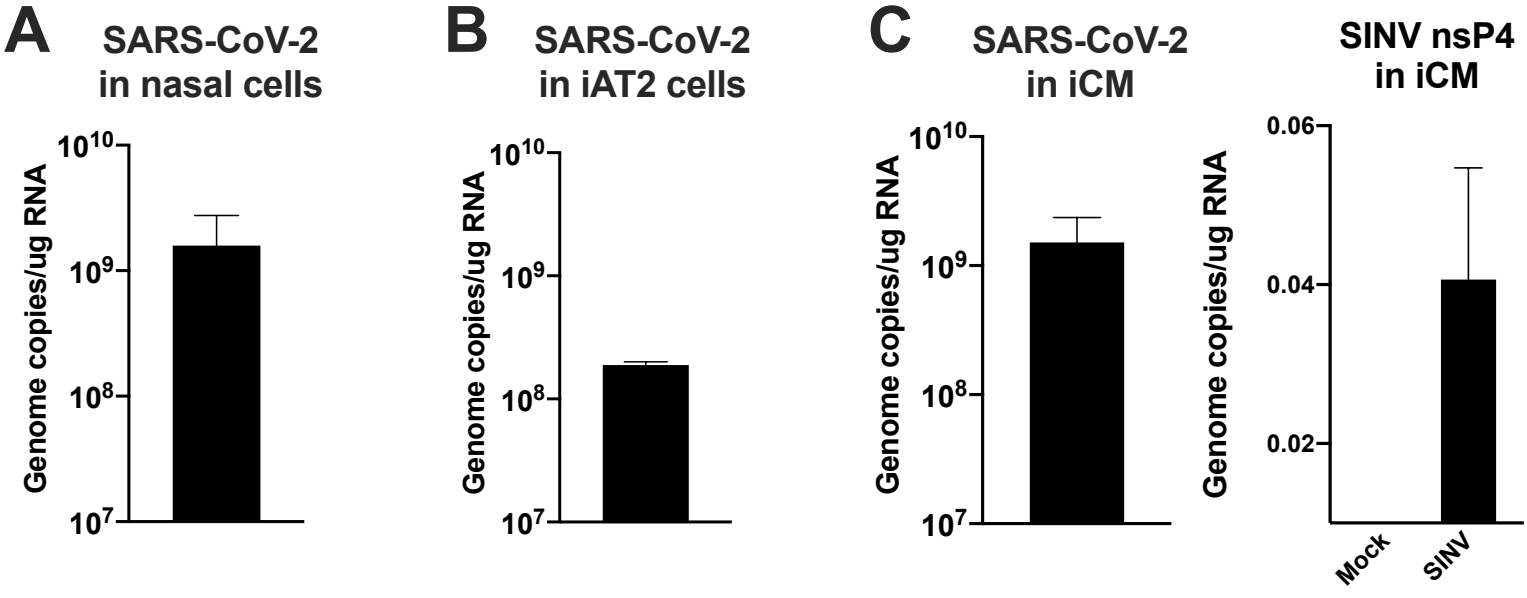
A
SARS-CoV-2
in nasal cells
Genome copies/ug RNA
$10^{10}$
$10^{9}$
$10^{8}$
$10^{7}$
B
SARS-CoV-2
in iAT2 cells
Genome copies/ug RNA
$10^{10}$
$10^{9}$
$10^{8}$
$10^{7}$
C
SARS-CoV-2
in iCM
Genome copies/ug RNA
$10^{10}$
$10^{9}$
$10^{8}$
$10^{7}$
SINV nsP4
in iCM
Genome copies/ug RNA
0.06
0.04
0.02
Mock
SINV

# Figure S1

A

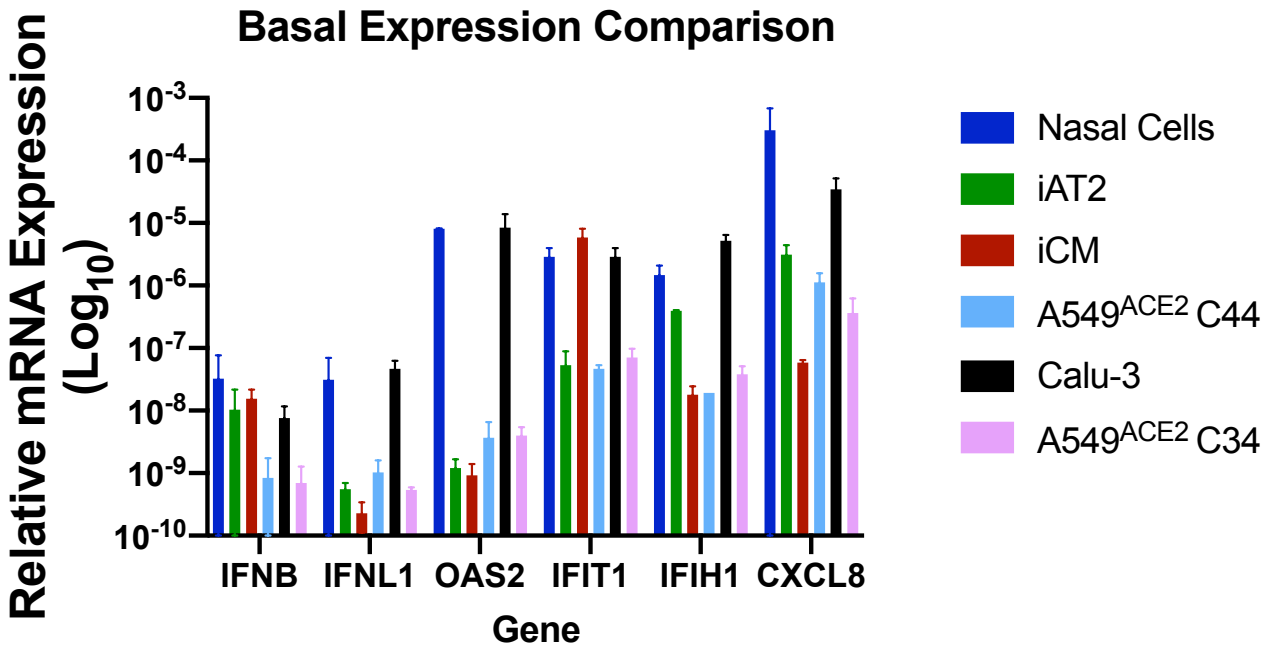
Basal Expression Comparison
Relative mRNA Expression (Log10)
10-3
10-4
10-5
10-6
10-7
10-8
10-9
10-10
IFNB
IFNL1
OAS2
IFIT1
IFIH1
CXCL8
Gene
Nasal Cells
iAT2
iCM
A549ACE2 C44
Calu-3
A549ACE2 C34

B

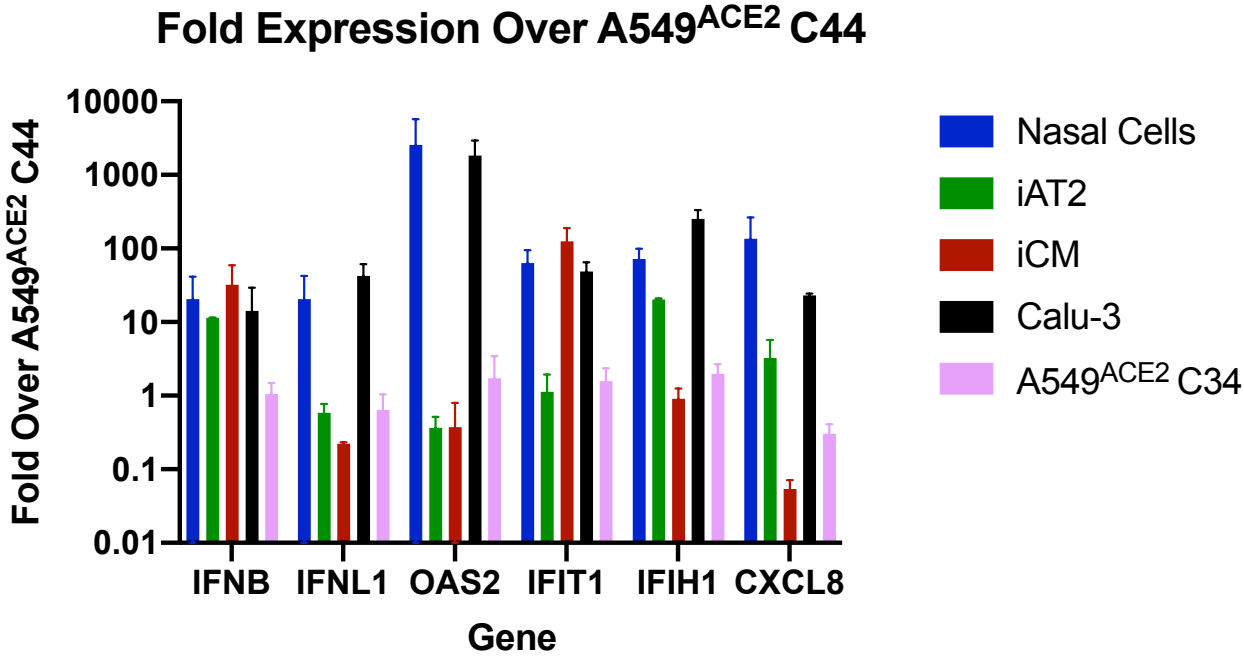
Fold Expression Over A549ACE2 C44
Fold Over A549ACE2 C44
10000
1000
100
10
1
0.1
0.01
IFNB
IFNL1
OAS2
IFIT1
IFIH1
CXCL8
Gene
Nasal Cells
iAT2
iCM
Calu-3
A549ACE2 C34

**Figure S2**

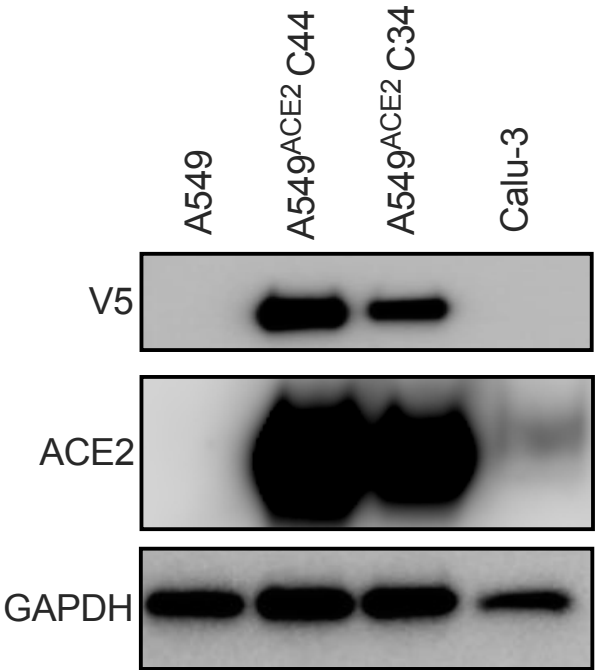


**Figure S3**

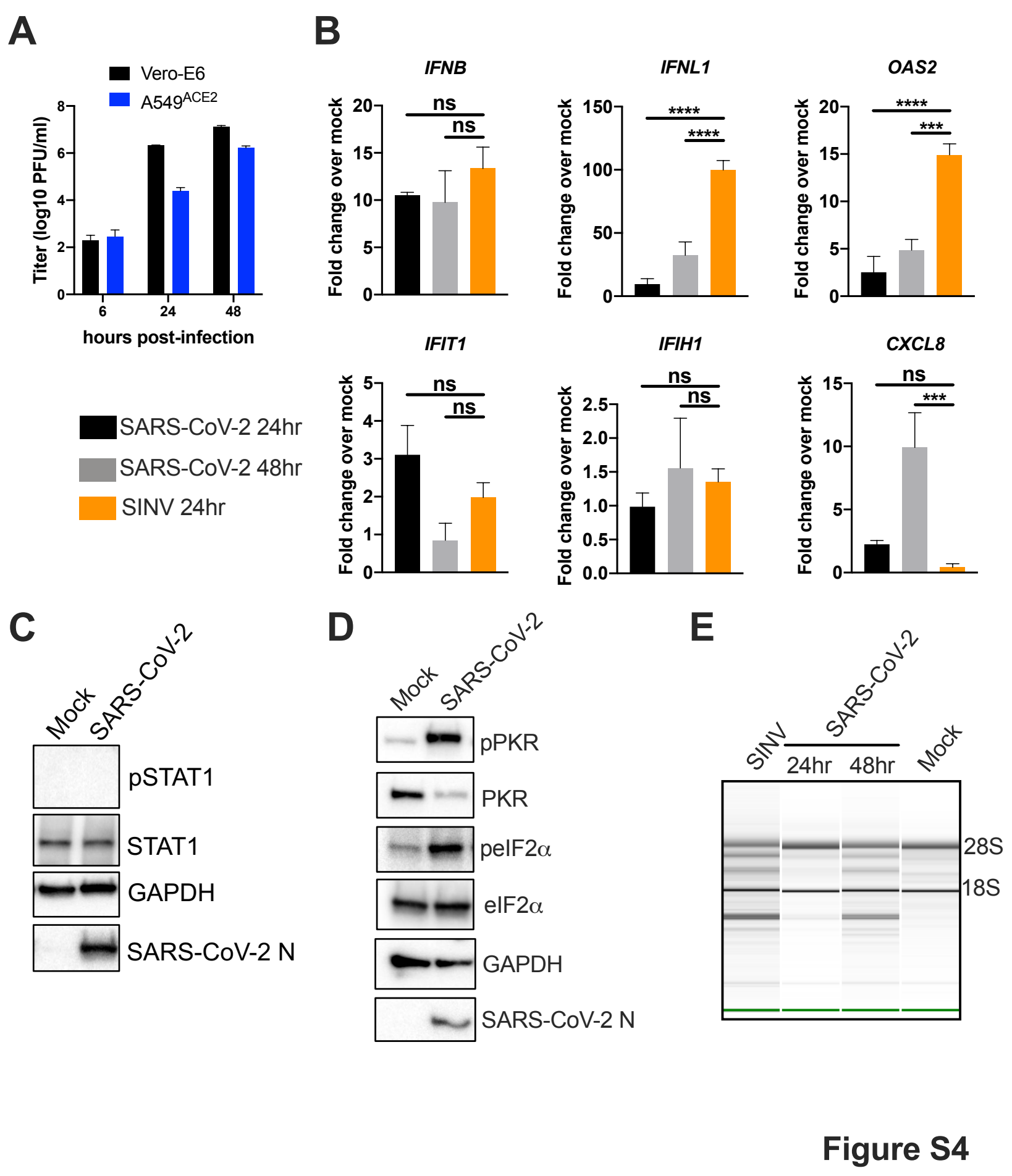
A
Vero-E6
A549ACE2
Titer (log10 PFU/ml)
hours post-infection
B
IFNB
IFNL1
OAS2
IFIT1
IFIH1
CXCL8
Fold change over mock
ns
****
***
SARS-CoV-2 24hr
SARS-CoV-2 48hr
SINV 24hr
C
Mock
SARS-CoV-2
pSTAT1
STAT1
GAPDH
SARS-CoV-2 N
D
pPKR
PKR
peIF2α
eIF2α
GAPDH
SARS-CoV-2 N
E
SINV
24hr
48hr
Mock
28S
18S

Figure S4